Journal Pre-proof

16pdel lipid changes in iPSC-derived neurons and function of FAM57B in lipid metabolism and synaptogenesis

Danielle L. Tomasello, Jiyoon L. Kim, Yara Khodour, Jasmine M. McCammon, Maya Mitalipova, Rudolf Jaenisch, Anthony H. Futerman, Hazel Sive

PII: S2589-0042(21)01521-2

DOI: https://doi.org/10.1016/j.isci.2021.103551

Reference: ISCI 103551

To appear in: *ISCIENCE*

Received Date: 1 April 2021

Revised Date: 23 September 2021

Accepted Date: 26 November 2021

Please cite this article as: Tomasello, D.L., Kim, J.L., Khodour, Y., McCammon, J.M., Mitalipova, M., Jaenisch, R., Futerman, A.H., Sive, H., 16pdel lipid changes in iPSC-derived neurons and function of FAM57B in lipid metabolism and synaptogenesis, *ISCIENCE* (2022), doi: https://doi.org/10.1016/j.isci.2021.103551.

16pdel lipid changes in iPSC-derived neurons and function of FAM57B in lipid metabolism and synaptogenesis

Danielle L. Tomasello[1], Jiyoon L. Kim[2], Yara Khodour[2], Jasmine M. McCammon[1], Maya Mitalipova[1], Rudolf Jaenisch[1,3], Anthony H. Futerman[2] and Hazel Sive[1,3*#]

[1]Whitehead Institute for Biomedical Research, Cambridge, MA 02142, USA.

[2]Department of Biomolecular Sciences, Weizmann Institute of Science, Rehovot, 76100, Israel.

[3]Department of Biology, Massachusetts Institute of Technology, Cambridge, MA 02139, USA.

*Present address: Northeastern University College of Science, Boston, MA 02115, USA.

[#]To whom lead contact should be addressed at: 115 Richards Hall, 360 Huntington Ave, Boston MA 02115, USA. Tel: (617) 373-5085; Email: h.sive@northeastern.edu

Summary

The complex 16p11.2 Deletion Syndrome (16pdel) is accompanied by neurological disorders, including epilepsy, autism spectrum disorder and intellectual disability. We demonstrated that 16pdel iPSC differentiated neurons from affected people show augmented local field potential activity and altered ceramide-related lipid species relative to unaffected. *FAM57B*, a poorly characterized gene in the 16p11.2 interval, has emerged as a candidate tied to symptomatology. We found that FAM57B modulates ceramide synthase (CerS) activity, but is not a CerS per se. In *FAM57B* mutant human neuronal cells and zebrafish brain, composition and levels of sphingolipids and glycerolipids associated with cellular membranes are disrupted. Consistently, we observed aberrant plasma membrane architecture and synaptic protein mislocalization, which were accompanied by depressed brain and behavioral activity. Together, these results suggest that haploinsufficiency of *FAM57B* contributes to changes in neuronal activity and function in 16pdel Syndrome, through a crucial role for the gene in lipid metabolism.

Introduction

16p11.2 Deletion (16pdel) Syndrome, a severe and prevalent neurodevelopmental disorder, is a copy number variant with deletion of ~600 kb from chromosome 16, encompassing 25 core protein-coding genes. This haploinsufficiency syndrome is estimated to affect ~1 in 2500 worldwide and is tightly associated with autism spectrum disorder (ASD), language and intellectual disability, seizures, attention-deficit/hyperactivity disorder, macrocephaly, hypotonia and obesity (D'Angelo et al., 2016, Hanson et al., 2015, Zufferey et al., 2012, Egolf et al., 2019, Maillard et al., 2015). Strong indications of synaptic defects are associated with 16pdel symptoms, particularly epilepsy (Fetit et al., 2020, Kleinendorst et al., 2020) and ASD (Fetit et al., 2020, Kim et al., 2020, Maillard et al., 2015, Ouellette et al., 2020, Sebat et al., 2007, Pinto et al., 2010, Zufferey et al., 2012), as well as links to metabolic defects (Hoytema van Konijnenburg et al., 2020).

Previously, analysis in the zebrafish model suggested that *FAM57B* is a pivotal hub gene in the 16p11.2 interval, that encodes a protein proposed to be a ceramide synthase (Yamashita-Sugahara et al., 2013). Using a pairwise partial loss of function screen for zebrafish embryonic brain morphology, we found that *fam57b* interacted with numerous other 16p11.2 interval genes, suggesting haploinsufficiency of *FAM57B* is critical in 16pdel Syndrome etiology (McCammon et al., 2017). FAM57B (family with sequence similarity 57, member B) is a Tram-Lag-CLN8 (TLC) family member, containing a domain of roughly 200 amino acids found in several other proteins, including ceramide synthases (CerS, the Lag of TLC) (Pewzner-Jung et al., 2006). Ceramides are sphingolipids (SLs) which are key membrane components and also act as signaling molecules to modulate proliferation, apoptosis, inflammation, cell cycle arrest and ER stress (Grosch et al., 2012). In humans, mutations in some of the 6 known CerS are associated with autism, epilepsy and intellectual disability (Vanni et al., 2014, Egawa et al., 2015, Ranta et al., 1999). In this study, to further assess the predicted connection with 16pdel Syndrome, we examined FAM57B function through a multidisciplinary approach, across human cells and the zebrafish system.

Results

Augmented network activity in 16pdel neuron cultures

Based on previous data, we hypothesized that 16pdel neurons would show an altered lipid profile due to contributions of *FAM57B* and possibly other 16pdel genes with predicted roles in metabolism (McCammon et al., 2017). To test this, we prepared neurons from 16pdel carrier induced-pluripotent stem cells (iPSC), part of the Simons VIP Consortium, and unaffected control iPSC in culture (Simons Vip, 2012) (**Supp Table 1**). Neural progenitor cells were differentiated into cortical neurons, since the cortex has consistently shown anatomical differences in 16pdel affected individuals (Martin-Brevet et al., 2018, Maillard et al., 2015, Hinkley et al., 2019, Lin et al., 2015, Qureshi et al., 2014, Blackmon et al., 2018). After one month in culture, immunocytochemistry (ICC) indicated mature neurons by presence of vesicular glutamate 1 and 2 receptors (VGlut1/2) (**Supp Figs. 1a,b**), the synaptic markers PSD95 (**Supp Fig. 1b**) and Synaptotagmin-1 (Syt1). Cultures of control and 16pdel (proband) differentiated neurons showed similar percentages of mature neurons by these criteria. Quantitative analysis was performed to determine equivalent maturation between control and 16pdel differentiated neurons. Production of synaptic proteins was measured by colocalization analysis, indicating neuronal somas that were Synaptotagmin-1 positive additionally colocalized with PSD-95 (**Supp Table 2**).

To further characterize these neurons, we probed network electrical activity by multi-electrode array (MEA). Spontaneous activity of differentiated neurons was measured over thirty minutes; first in culture media, followed by physiological solution and last in high potassium chloride solution. Comparing grouped genotypes, we recorded an increased frequency of Local Field Potentials (LFPs) in 16pdel proband neuron cultures relative to controls, indicating 16pdel neurons display heightened spontaneous and evoked activity compared to unaffected control (**Fig. 1a**). Examining individual patient cell lines, we observed relatively similar MEA

activity in controls (black), and increased electrical activity in 16pdel neuron cultures (grey) (**Supp Fig. 2a**). Interestingly, female 16pdel neuron cultures showed statistically increased LFP frequency compared to male 16pdel neuron cultures when measured in media and High KCl solution (**Fig. 1b**). Sex differences were also observed in LFP firing and bursting properties, with increased burst frequency of female 16pdel neurons compared to male in media (**Fig. 1c**). While behavioral deficits have been widely observed among male mouse 16pdel models, a recent report found stress-related sex differences in a female 16p11.2 deletion mouse model. Thus, Giovanniello *et al.* discovered an increase in activity in central amygdala neurons projecting to the globus pallidus in female, but not male, 16pdel model mice (Giovanniello, 2021). Our data consistently suggest sex-specific differences between activity of 16pdel and control neurons. These findings expand previous observations that demonstrated larger cell size and deficits in synaptic density in 16pdel neurons compared to control (Deshpande et al., 2017).

Significant lipid class and individual species changes indicates complexity of 16pdel Syndrome.

Using differentiated 16pdel and control neurons, we compared their lipid cohorts using untargeted lipidomics (**Table S1 - iPSC Neuron Lipidomics**). Consistent with predictions, many significant changes were observed in total lipid classes between 16pdel and control neurons (**Fig. 2a**). Levels of SLs (ceramide (Cer) and sphingomyelin (SM)) and glycerolipids (GL) (lysophosphatidylethanolamine (LPE), phosphatidylethanolamine (PE), monoacylglycerol (MG)) were significantly decreased, while GL (triacylglycerol (TG)) levels significantly increased. Analyzing lipid composition, we found similar levels of unsaturated and saturated species between 16pdel and control neurons, but differences in saturation of acyl carnitine (AcCa) (unsaturated control 33.78% vs 16pdel 55.16%, and saturated control 66.22% and 16pdel 44.84%) and TG (unsaturated control 71.15% vs 16pdel 80.28%, and saturated control 28.85% and 16pdel 19.72%) (**Fig. 2b**). Polyunsaturated fatty acids (PUFAs) are important in the brain, where they are essential for signaling and membrane structure (Bazinet and Laye, 2014). Chain length analysis indicated large differences in lysophosphatidylglycerol (LPG) (long chain control 85.76% vs 16pdel 75.55%) and phosphatidylglycerol (PG) (long chain control 71.78% vs 16pdel 51.88%). While having a similar ratio of long and very long chain PE species (**Fig. 2b**), analysis of individual lipid species demonstrated significantly decreased levels of several PE(18:22) species in 16pdel neurons relative to control (**Fig. 2c**). Additionally, decreased Cer(18) species were observed in 16pdel (**Fig. 2d**). Comparing MG and TG, MG(18:0) decreased while many TG(18:1,18:2,18:3) increased (**Fig. 2e,f**). Together, this analysis identifies differences in metabolism of ceramides and GLs in 16pdel neurons that are critical for function of the ER, mitochondria and plasma membrane (Flis and Daum, 2013). The shift in saturation and tail length of GLs between 16pdel and control neurons suggests a dysfunctional neuronal membrane.

FAM57B functions as a ceramide synthase modulator

We considered that the extensive lipid differences between 16pdel and control neurons may partly result from FAM57B activity. The function of this protein is not clear, although a single report suggests that FAM57B has ceramide synthase activity (Yamashita-Sugahara et al., 2013). However, sequence analysis indicates that while FAM57B is part of the TLC protein family, including ceramide synthases (CerS), FAM57B has little sequence similarity to CerS, even in the TLC domain (**Supp Fig. 3**). To assess whether FAM57B is a *bone fide* CerS, it was expressed in *CerS2*$^{-/-}$ *(KO)* HEK293T cells, which lack endogenous CerS2 activity (Tidhar et al., 2012) (**Fig. 3a**). No CerS2 activity was detected in *CerS2 KO* cells upon transfection of FAM57B alone. However, co-transfection of FAM57B with CerS2 resulted in a significant increase in CerS2 activity compared to transfection of CerS2 alone (**Fig. 3a**), suggesting that FAM57B might modulate CerS2 activity. There are six CerS isoforms in mammals, where each uses a restricted subset of acyl CoAs of defined chain length for ceramide synthesis(Levy and Futerman, 2010). To assess whether FAM57B can modulate other members of the mammalian CerS family; we expressed CerS5 and CerS6 with or without co-transfection of FAM57B in wildtype HEK293T cells. Upon co-transfection of CerS2 with FAM57B in wildtype HEK293T cells, levels of CerS2 activity and expression were significantly increased compared to CerS2 alone (**Fig. 3b**). While co-transfection of FAM57B with CerS5 did not alter expression nor activity of this CerS (**Fig. 3c**), an opposite trend was seen upon co-transfection of FAM57B with CerS6, whose activity decreased upon co-transfection with FAM57B (**Fig. 3c**). These results suggest that FAM57B affect protein levels and activity of certain CerS isoforms, and may do so by an indirect mechanism, dependent on interaction of the two proteins. This hypothesis was confirmed by immunoprecipitation, in which Flag-tagged FAM57B was able to interact with all three HA-tagged CerS isoforms (**Fig. 3d**). These data newly implicate FAM57B as a modulator of CerS, but refute a previous report that this protein functions as a CerS (Yamashita-Sugahara et al., 2013).

FAM57B **modulates lipid cohorts and synaptic proteins in human cells**

The intriguing functional differences between 16pdel and control neurons raises the question of whether *FAM57B* haploinsufficiency contributes to these differences. To address this, we used the human neuroblastoma line SH-SY5Y to create knockout (*FAM57B KO*) and *FAM57B* heterozygote (*FAM57B HET*) lines, using CRISPR-Cas9 editing. SH-SY5Y cells have proven useful for studying neuronal properties and function (Kovalevich J, 2013). After confirmation of CRISPR induced genome editing by next generation sequencing, FAM57B protein depletion was confirmed by western analysis (**Supp Fig. 4**). For our studies, SH-SY5Y cells were differentiated into neurons after incubation in media containing retinoic acid. Overall, total lipid classes showed significant differences between *FAM57B KO* and WT (wildtype), specifically, increased ChE and MG (**Fig. 4a**, **Table S2 - SH-SY5Y Lipidomics)**. Comparing *FAM57B HET* to WT, we observed increased LPC (**Fig. 4b**). Additionally, relative to *FAM57B HET*, we found HexCer and PG significantly decreased while ChE increased in *FAM57B KO* cells (**Fig. 4c**).

Notably, lipid class differences observed between *FAM57B KO*, *FAM57B HET* and WT were similarly altered in 16pdel patient neurons compared to controls (**Fig. 2a**). This, in both *FAM57B KO* and *FAM57B HET*

relative to WT, we observed increased abundance of PE(18:0,18:1,22:4,22:5) (**Fig. 4d**), Cer(d18:1) (**Fig. 4e**), MG(18:0) (**Fig. 4f**), and with decreased abundance of TG(16:0,16:1,18:0,18:1,18:2,22:6) (**Fig. 4g**). These differences are similar to those seen in 16pdel relative to control neurons (**Fig. 2c-f**). In *FAM57B KO* relative to WT, there was increased abundance of MG and decreased abundance TG (**Fig. 4f,g**), as for 16pdel neurons compared to control (**Fig. 2a,e,f**). The alterations in lipid cohorts between *FAM57B KO* and *FAM57B HET* human neurons is similar to lipid changes in 16pdel neurons compared to control, and consistent with a role for FAM57B in dosage-sensitive lipid regulation. The similarities in lipid cohort alterations between *FAM57B KO* compared to *FAM57B HET* in SH-SY5Y human neurons and 16pdel neurons, is consistent with a role for FAM57B in dosage-sensitive, lipid regulation, including tight regulation of HexCer (**Fig. 4c**).

To understand the consequence of *FAM57B loss of function* on neuronal maturation and function, we probed synaptic composition. Synaptosomes, comprising the pre- and postsynaptic membranes and postsynaptic density, were isolated from unfixed cells and processed by MS/MS (**Table S3 - SH-SY5Y Synaptosome MSMS)**. Synaptosomes from *FAM57B KO* cells showed significantly decreased abundance of over 100 proteins relative to WT (**Fig. 5a**). In contrast, *FAM57B HET* showed no statistically significant changes in synaptosome protein composition relative to WT (**Fig. 5b**), with the exception of Dopamine Beta-Hydroxylase (DBH). Among the top 20 significantly decreased proteins in the *FAM57B KO* synaptosomes were those associated with protein trafficking, localization and stabilization (**Fig. 5c,d**). Additionally, we observed an overall decrease in levels of hallmark synaptic proteins in *FAM57B KO* compared to *FAM57B HET* or *WT* (**Fig. 5e**). These decreases included α-internexin INA, small GTPase vesicle recycling RAB11B, SNARE protein syntaxin STXBP1 and scaffolding protein YWHAZ. INA is a neurofilament subunit protein important for neuronal cytoskeletal assembly and synaptogenesis localized to the post-synaptic terminal (Yuan and Nixon, 2016).

Separately, synaptosomes were isolated from differentiated SH-SY5Y cells and processed for lipidomic analysis (**Table S4 - SH-SY5Y Synaptosome Lipidomics)**. Comparing lipids localized to the pre- and post-synaptic terminals between *FAM57B KO* to WT neurons, significant changes in lipid abundances were observed, notably in hexosylceramide (HexCer) and monoacylglycerol (MG) (**Fig. 5f**). Relative to WT, Hex2Cer and MG abundances increased, while Hex1Cer and phosphatidic acid (PA) abundances decreased. No statistically significant changes in lipid group abundances were observed between *FAM57B HET* relative to WT or *FAM57B KO*. These results suggest altered lipid composition, due to loss of *FAM57B* function at developing synapses impacts localization and/or trafficking of synaptic proteins in *FAM57B* mutant neurons. Together, the data indicate that in human neurons mutant or heterozygous for *FAM57B,* there are significant changes in lipid composition and regional synaptic protein abundance. The data are consistent with the suggestion that a deficit in FAM57B function partly contributes to 16pdel neuronal anomalies relative to control. The smaller changes observed in *FAM57B HET* relative to *FAM57B KO* suggests that other 16pdel genes contribute to phenotypes in the haploinsufficient syndrome.

FAM57B is essential for Sphingolipid (SL) and Glycerolipid (GL) homeostasis in the developing brain.

16pdel alters brain structure and function, including neuroanatomical abnormalities and increased risk of psychiatric and other brain disorders (Niarchou et al., 2019, Owen et al., 2018). To understand how *FAM57B* contributes to brain development, we analyzed zebrafish, *Danio rerio*, a powerful system for analysis of neural development and neurodevelopmental disorders (Kalueff et al., 2014, Stewart et al., 2014, Xi et al., 2011, McCammon and Sive, 2015). The zebrafish genome includes two copies of the *fam57b* gene, *fam57ba* and *fam57bb*. We used CRISPR to build double (null) mutants, *fam57ba*$^{-/-}$;*fam57bb*$^{-/-}$ (*fam57b mut*), and heterozygotes *fam57b*$^{+/-}$;*fam57bb*$^{+/-}$ *(fam57b het)*, to assess dosage effects of FAM57B.

To determine whether *fam57b* regulates lipid metabolites, we performed untargeted lipid profiling on *fam57b mut* and *fam57b het* zebrafish brain tissue at 7 days post-fertilization (7 dpf), an optimal timepoint for molecular and behavioral studies of a developing yet complex brain (**Table S5 - Zebrafish Larvae Brain Lipidomics)** (Tomasello and Sive, 2020). Striking differences in SL and GL lipid abundances were present in *fam57b mut* and *fam57b het* compared to wildtype (AB) zebrafish brain (**Fig. 6a,b**). By lipid class, there was a significant increase in Cer, LPE, MG and SM along with phosphatidylinositol (PI) and cardiolipin (CL) and decreased PS in *fam57b mut* compared to AB (**Fig. 6a**). A similar trend to *fam57b mut*, with increased hexosylceramide (HexCer) and decreased PS lipid classes, were defined in *fam57b het* brains compared to AB control. An overlap in lipid differences were observed between *fam57b mut* brains and FAM57B KO human neurons, with increased abundance of MG class, and Cer(d18:1) and MG(18:0) species (**Figs. 6a, 4a, 6d,e, 4d,e**). Many PE species similarly increased, PE(18:0,18:1,20:4), comparing *fam57b mut* and *FAM57B KO* to controls. An important finding across all systems compared, including 16pdel syndrome patient neurons, heterozygous and mutant *FAM57B* cells and larvae brains, is a change in ether-linked PE (**Figs. 2c, 4d, 6c,g**). Ether GLs differ in phase-transition temperature from gel to liquid crystalline and from lamellar to hexagonal phases, and are proposed to regulate properties of neuronal membranes (Paltauf, 1994, Lohner, 1996). In addition to PE, ceramides were altered in *fam57b mut* and *fam57b het* brain tissue compared to AB (**Fig. 4d,h**). Lipidomics resolved predominantly Cer(d18:1) species in zebrafish brains, which agrees with previously published ceramide composition at 7 dpf (Zhang et al., 2019). These findings suggest a key role for Fam57b in SL and GL regulation during brain development.

These data demonstrate that *fam57b* is crucial for regulation of SL and GL classes in the larval zebrafish brain, and that there is a gene dosage-dependent effect. The data in zebrafish brain are quite similar to changes seen in human neurons after FAM57B knockout (**Fig. 4**). These changes affect comparable lipid groups to those altered in 16pdel neurons relative to control, although they are not the same. For example, LPE significantly decreased in the 16pdel neurons (**Fig. 2a**), while the class remained unchanged or significantly increased in the *fam57b* het and null SH-SY5Y cells (**Fig. 4a-c**) and zebrafish brain (**Fig. 6a,b**), suggesting additional genes regulate 16pdel lipid metabolites or that these result from other differences between the tissue being compared.

Changes in plasma membrane and associated proteins in *fam57b mut* and *fam57b het* brains

Ceramide, hexosylceramide and GL species are integral to membrane composition, are differentially distributed across inner and outer leaflets of the plasma membrane and contribute to lipid rafts (Kraft, 2016). Given the changes in these lipids observed in *fam57b mut* brains, we predicted that plasma membrane structure would also be altered. To assess lipid raft organization, fluorophore-conjugated Cholera Toxin subunit B (CT-B), which binds ganglioside GM1 found in lipid rafts (Fishman et al., 1978), was injected into the hindbrain ventricle of *fam57b mut* and AB zebrafish embryos at 24 hours post fertilization (hpf), when ventricles are accessible for injection (Worstell et al., 2016) (**Fig. 7a**). Embryos fixed after 1-hour incubation demonstrated a significant increase in punctate GM1 labeling in neural progenitor cells of *fam57b mut* brains compared to AB (**Fig. 7b**). To asses changes in glycerophospholipid species in plasma membranes, we stained with duramycin, a label for membrane PE (Marconescu and Thorpe, 2008). Mutant progenitors showed statistically increased punctate PE staining, indicating altered PE localization that could impact membrane architecture (**Fig. 7c**). The duramycin puncta may indicate exosomes or extracellular vesicles containing PE (Beer et al., 2018). At 24 hpf, we did not observe changes in cell proliferation or cell death between *fam57b mut* and AB (**Supp. Fig 5**). The data suggest that there is alteration in the plasma membrane of *fam57b mut* brains relative to AB.

The changes in membranes of neural progenitor cells suggested that membrane protein localization may also be altered. We therefore examined localization of membrane by biotinylation analysis. Freshly dissected larval brains from *fam57b mut* or AB at 7 dpf were incubated with membrane impermeable biotin. Surface proteins were affinity-purified and quantified by MS/MS (**Fig. 7d**, **Table S6 - Zebrafish Larvae Brain Biotinylation MSMS)**. MS/MS analysis indicated that membrane-associated protein cohorts were similar between *fam57b mut* and AB brains (**Fig. 7e**), however, a small group of proteins showed altered abundance. In *fam57b mut* brains, the protein whose levels most significantly decreased (2-fold) relative to AB was Synaptotagmin-1a (Syt1) (**Fig. 7e**). Syt1a, homologous to human SYT1, is a vesicle membrane protein that acts as a calcium sensor and regulates synaptic and endocrine vesicle exocytosis (Fernandez et al., 2001, Sorensen et al., 2003, Xu et al., 2007, Gustavsson and Han, 2009, Schonn et al., 2008). Syt1 protein domains interact with the lipid bilayer, including GL PS that are altered in *fam57b mut* and *fam57b het* (**Fig. 5a,b**). Mammalian Syt1 can modify PS, and is able to alter curvature strain on the membrane (Lai et al., 2011).

To investigate the decreased membrane abundance of Syt1 in the biotinylation assay, we performed immunostaining on 7 dpf larvae brains (**Fig. 7f**). Whole larval brains were cleared and tertiary structure was protected using SHIELD protocols. Slice imaging of dorsal brain view showed that Syt1 protein was largely confined to projections of neurons throughout the AB brain, both GABAergic (GAD65/67) and non-GABAergic, while *fam57b mut* brains showed ectopic expression throughout the brain (**Fig. 7f**). By western blot, we found no change in total brain Syt1 between *fam57b mut* and AB, suggesting that immunostaining demonstrates Syt1a mislocalization (**Fig. 7g, Supp Fig. 6**). Imaging also revealed anatomical changes in the larval *fam57b mut* brain, including tectum and corpus cerebelli (**Fig. 7f**).

Together, these results indicate that in the brain, relative to wildtype, *fam57b mut* animals show changes in lipids, membrane structure and membrane protein association, including the synaptic regulator Syt1 and others functioning at synapses. The data indicate that *fam57b* is required for membrane structure and neuronal architecture.

Pre- and post-synaptic proteins depleted after loss of *FAM57B*

To examine the implications of Syt1 mis-localization on synaptic composition, we isolated synaptosomes from freshly dissected and unfixed brains of *fam57b mut* or AB larvae (**Table S7 - Zebrafish Larvae Brain Synaptosome MSMS)**. Proteomic profiling indicated a group of proteins whose representation significantly increased, and another larger group whose representation significantly decreased in *fam57b mut* compared to AB (**Fig. 7h**). Interestingly, we observed a decrease of the Synaptotagmin family member Syt2a-like protein, similar to human SYT2, with analogous function to SYT1. Gene ontology (GO-Slim and Panther Protein Class ontology) defined synaptic protein groups found only in the decreased synaptosome protein group (**Fig. 7i, 7j**). Annotations in the decreased group included synapse and synapse part components, cytoskeletal and membrane traffic proteins, biological adhesion, development and signaling, and numerous implicated pathways including synaptic vesicle trafficking. These results indicate that synaptic protein levels were significantly altered in synaptosomes from *fam57b mut* larval brain synapses relative to AB.

We separately examined levels of synaptotagmin family members in brain synaptosome profiles and found decreased Syt1 and Syt2a protein levels in *fam57b mut* compared to AB synaptosomes (**Fig. 7k**). This interesting association between FAM57B regulation and Synaptotagmin expression (**Fig. 7e,f,h**) led us to analyze further human SH-SY5Y isolated synaptosomes. We found a significant decrease in elongated SYT1 (ESYT1) in *FAM57B KO* compared to *FAM57B HET* and WT (**Fig. 7l**), a calcium activated synaptic protein found to bind GLs (Yu et al., 2016). We then characterized hallmark proteins that function at the synapse from brain synaptosomes, including synaptic vesicle fusion and tethering proteins. Bayés *et al.* previously examined complexity of the adult zebrafish synapse proteome relative to adult mouse synapse proteome (Bayes et al., 2017). As expected, not all synaptic proteins were detected at this immature stage of zebrafish development compared to the adult brain. Enrichment of synaptic vesicle proteins including Syntaxins, Slc neurotransmitter transporters, SNAPs, Stx/Vps, Synaptotagmins and membrane budding proteins including Dynamins and Rabs verify synaptosome isolation and give new data regarding neuronal maturation in the zebrafish larval brain (**Fig. 7j**). Comparison of synaptic protein profiles between genotypes demonstrated decreased vesicle fusion and transport protein Nsfa, ligand-gated ion channel Si:ch211-251b21.1, and SNARE complex proteins Snphb, Stx1b, Stxbp1a and Vamp3 (**Fig. 7j**). Together, these data show that synaptic proteins essential for vesicle docking, exo- and endocytosis, including synaptotagmin family members, are diminished in synaptosomes isolated from *fam57b mut* brains relative to AB, suggesting Fam57b is essential for synapse integrity.

Depressed spontaneous electrical activity and response to stimuli in *fam57b* mutants

To understand how changes in *fam57b* gene dosage impact neuronal activity, we tested brain activity by electrophysiological analysis. We previously described a noninvasive electrophysiology technique that can be used in live larvae to measure spontaneous activity in the brain and spinal cord (Tomasello and Sive, 2020). Using a multielectrode array (MEA), we measured local field potential (LFP) parameters and relative coordinated (network) activity in the brain of 7 dpf larvae (**Figs. 8a-c**). Larva were individually immersed in precooled 1.5% low-melt agarose in E3 solution and mounted in a 64-electrode containing well. We measured spontaneous brain activity over a 10-minute period, comparing *fam57b mut* to AB controls. Only electrodes in contact with the larval head were analyzed, ~6 to 8 electrodes, whose signal was pooled. *fam57b mut* larvae had slightly smaller heads than AB at 7 dpf (**Supp Fig. 7**, **Table S8 - Zebrafish Larvae Head and Body Measurements)**, however these changes do not impact electrophysiological studies. Overall, *fam57b mut* spontaneous brain activity was severely diminished relative to ABs. This included significant decrease in number of LFPs, mean LFP rate, and inter-LFP-interval coefficient of variation measurements, indicating decreased spontaneous brain activity with reduced kinetics (**Fig. 8a**). However, the decreased coefficient of variation in the *fam57b mut* suggests LFP interval distributions are detected at a more regular rate. Measuring electrographic bursts, at least 5 LFPs per 100 ms, we were unable to detect any burst activity under these settings in the *fam57b mut*, while bursts were detected in ABs. To increase sensitivity for detection of burst activity, we lowered the detection parameters to at least 3 LFPs per 200 ms (right column), and found decreased electrographic burst duration, number of LFPs per burst, burst frequency and percentage in *fam57b mut* relative to AB (**Fig. 8a**). In addition, we examined relative network activity, as defined by at least 3 LFPs detected simultaneously between a minimum of two electrodes. Relative network activity was also significantly decreased in *fam57b mut* compared to AB. Synchrony index of bursts did not change between the two genotypes, indicating coordination of network activity did not differ. While LFP waveforms could not be quantified due to small distance variations when mounting individual larva, we observed smaller relative waveforms in *fam57b mut* compared to AB (**Fig.8c**), consistent with overall decreased brain activity in *fam57b mut* larvae. A representative raster plot of LFP activity in the head region over the 10-minute recording period illustrates the relative decrease in LFP propagation, burst and network detection measured (**Fig. 8d**). A representative image of a mounted larva immersed in agarose on a 12-well 64 electrode plate is shown in **Fig. 8e**. These data demonstrate severely diminished spontaneous brain activity in *fam57b mut* relative to AB wildtype larvae, and highlight a role for Fam57b in regulating brain function.

After identifying significantly diminished spontaneous brain activity in *fam57b mut* larvae, we examined correlations with behavioral activity. We first tested light-responsive sensorimotor startle behavior (**Table S9 - Zebrafish Larvae Light Startle Response Data)**. Startle response, as indicated by distance traveled, was measured over a 70-min time-frame with light extinguished every 10 minutes for 5 seconds (Tomasello and Sive, 2020). The startle response window was in total 30 seconds, including the stimulus. We found a considerable decrease in response to each light stimulus in *fam57b mut* compared to AB (**Fig. 8f**). However, movement measured previous to startle (first 10 min) and relative habituation after startle cue did not overall

differ between the genotypes, indicating there is no alteration in movement outside of the light stimulus, and no visual deficit in *fam57b mut* larvae.

To examine brain specific activity, we investigated seizure susceptibility (**Table S10 - Zebrafish Larvae Seizure Assay Data)**. Seizures are prevalent in individuals affected with 16pdel syndrome, and may result from processes involving several neurotransmitter systems, including glutamatergic, cholinergic and GABAergic (Mefford et al., 2011). To measure seizure propensity, larvae were immersed in pentylenetetrazol (PTZ), a $GABA_A$ antagonist, well characterized for use in zebrafish (Baraban et al., 2005). After a 10-minute baseline movement recording, two different concentrations of PTZ, or E3 media only control, were applied to the individual well of each larva and recorded over 10 minutes. There was no significant change in normalized movement, compared to baseline recording, in the absence of stimulus after addition of E3 (0 mM PTZ) control between the *fam57b mut* and AB (**Fig. 8g**). Increasing the PTZ dose increased normalized distance traveled for both genotypes, but the increase was not significant for AB between 0 and 0.5 mM PTZ as observed in *fam57b mut.* At 5 mM, we observed significantly less distance traveled in the *fam57b mut* compared to AB. However, the relative fold change between 0 and 5 mM was much higher in the *fam57b mut* (roughly 32-fold) compared to AB (roughly 11-fold). To understand the contribution of Fam57ba and Fam57bb to the seizure phenotype, we incrossed *fam57ba*$^{+/-}$*;fam57bb*$^{+/-}$ animals and measured seizure propensity in resulting genotypes (**Supp Fig. 8**). We found no statistical differences in baseline movement between AB control compared to *fam57ba*$^{-/-}$*;fam57bb*$^{-/+}$, *fam57ba*$^{-/+}$*;fam57bb*$^{-/+}$ nor *fam57ba*$^{-/+}$*;fam57bb*$^{+/+}$. The data are consistent with increased movement after addition of 5 mM PTZ in *fam57ba*$^{-/-}$*;fam57bb*$^{+/+}$ 7 dpf larvae compared to AB control (McCammon et al., 2017). The enhanced PTZ-responsiveness of *fam57b mut* relative to WT suggests that Fam57ba and Fam57bb function in GABA-mediated signaling with synergistic effects after the loss of Fam57bb in combination with Fam57ba. These analyses indicate neuronal specific changes after loss of *fam57b mut*, however, FAM57B is also expressed in muscle. We assessed neuromuscular junction contribution by immunostaining, but did not observe differences between *fam57b mut* and AB (**Supp. Fig. 9**). Together, altered brain activity, response to multiple stimuli including $GABA_A$ antagonist, and gross anatomical differences including the corpus cerebelli (**Fig. 7f**), suggest changes to GABAergic network activity in the developing *fam57b mut* brain.

In sum, there are significant behavioral changes in zebrafish larvae after *fam57b* loss of function. *fam mut* larvae move similarly to AB over time without a stimulus. However, with a stimulus – either dark or PTZ application, there is altered behavioral responsiveness relative to AB. These findings are consistent with changes in brain activity in *fam57b mut* relative to AB controls.

Discussion

This study has uncovered alterations of lipid metabolism in iPSC differentiated cortical neurons derived from people affected with 16pdel Syndrome, relative to unaffected. These 16pdel neurons display increased excitability relative to controls, and show a sex-linked difference. Among the set of twenty-five 16pdel genes,

FAM57B is a key candidate gene linked to symptomatology, and implicated in lipid metabolism. Consistently, we find changes in 16pdel neuronal lipids, as well as those in *FAM57B* mutants in a human neuronal cell line and zebrafish model. In *FAM57B* mutants, lipid alterations occur concomitantly with alterations in membrane architecture, synapse lipid composition synapse-associated proteins, and in zebrafish, altered brain activity and behavior. Specifically, we identified altered abundance of the monoacyglyerol (MG) group in all experimental conditions, including 16p11.2 deletion neurons and SH-SY5Y *FAM57B KO* intact neurons and isolated synaptosomes (**Figs. 2a, 4a, 5f, 6a**). We do not know how these outcomes are linked, but it is plausible that FAM57B acts through sphingolipid (SL) and glycerolipid (GL) regulation as the starting point for a cascade of effects after loss of function. Dysregulated lipid metabolism has a multifaceted effect on neurons, for example, increased lipid energy consumption escalates oxidative stress, promoting inflammation, mitochondrial and metabolic dysfunction and excitotoxicity (Tracey et al., 2018). The saturation and length of individual lipids affects their intracellular localization, impacting the cytoskeleton and lipid raft composition, so disrupting signaling processes that regulate neurotransmitter synthesis and release, cytoskeletal integrity, myelination and intracellular transport (Pike, 2003, Tracey et al., 2018). Abnormal cholesterol metabolism has been observed in patients with Asperger syndrome and other ASDs, suggesting a correlation between lipid raft formation and ASD (Dziobek et al., 2007, Tierney et al., 2006).

In contrast to a previous report (Yamashita-Sugahara et al., 2013), we find that FAM57B is not a ceramide synthase (CerS) but rather is a modulator of CerS activity. Supporting a functional interaction between FAM57B with CerS2 and CerS6, lipidomic profiling uncovered altered SLs and GLs integral to the lipid membrane in *FAM57B* mutants of both zebrafish brain and a human neuronal cell line, also indicating consistent activity of this gene across species. Comparing these mutants with 16pdel iPSC differentiated patient neurons, we identified a consistent change in ether-linked phosphatidylethanolamine (PE) species, supporting a role for *FAM57B* in the altered 16pdel lipidome relative to unaffected. However, some lipid groups altered in mutant human neuronal cells, zebrafish brain and 16pdel neurons relative to controls are do not overlap, suggesting additional genes regulate 16pdel lipid metabolites or that these result from other differences between tissues being compared. Beyond *FAM57B,* multiple genes in the 16p11.2 interval encode enzymes with predicted roles in metabolic processing or interconversion including *ALDOA, CDIPT, GDPD3, BOLA2, SULT1A3, SULT1A4* and YPEL3 (Giannuzzi et al., 2019, Arbogast et al., 2016). Together with FAM57B activity, this set of genes may function to modulate lipid metabolism.

Early in brain development, *fam57b* mutants displayed altered plasma membrane architecture, while in more mature neurons, synaptic proteins were present at significantly diminished levels in synaptosomes prepared from mutants relative to controls. One important affected protein in zebrafish brain was Syt1a, a member of the Synaptotagmin family and calcium sensor SNARE binding complex protein that contributes to synchronous synaptic vesicle release (Li et al., 2017). Baker-Gordon Syndrome, a SYT1-associated neurodevelopmental disorder, maps to an autosomal dominant heterozygous mutation of *SYT1,* that is associated with reduced neurotransmitter release (Baker et al., 2018). This association supports our previous

findings of a genetic interaction between *fam57ba* and *doc2a*, another 16p11.2 interval gene, encoding a calcium sensor SNARE binding complex protein for spontaneous vesicle release, where double heterozygotes showed hyperactivity and increased seizure propensity (McCammon et al., 2017). In further connections, ESYT1 is a related Synaptotagmin family member whose synaptic levels were diminished in human neuronal cell lines, that may play a role in cellular transport of PC, PE, PI, and translocates to sites of contact between the presynaptic endoplasmic reticulum and the cell membrane in response to increased cytosolic calcium levels (Yu et al., 2016). Neurotransmission is decreased in *Esyt D.melanogaster* mutants, with a proposed role in synapse extension, highlighting the essential homeostasis of lipids at the synapse (Kikuma et al., 2017).

Diminished spontaneous brain activity and altered behavioral response after stimulation seen in *fam57b* zebrafish mutants is consistent with alteration of brain synaptic composition. These studies suggest Fam57b is essential early in development of the brain, and loss of *fam57b* leads to linked events starting with changes in plasma membrane architecture followed by disturbance in protein organization at the membrane and detriments to basic neuronal function that impacts brain activity and behavior. Together, we propose a model whereby Fam57b functions to maintain normal plasma membrane physiology, necessary for proper formation and function of neurons (**Fig. 8h**).

In a recent study that analyzed the largest ASD-associated exome sequence to date (Satterstrom et al., 2019), 102 high risk genes were identified as tightly associated with ASD. In the analysis, a rare G:A mutation was discovered in *FAM57B,* located in the 5'UTR of one *FAM57B* transcript isoform, and residing in the promoter/enhancer region of the five other *FAM57B* isoforms. This synonymous mutation is predicted to create binding sites for several transcription factors and may impact enhancer activity in neurons, affecting gene expression (prediction with information from dbSNP, JASPAR, GTEx). The association of a single gene *FAM57B* mutation with ASD outside of the complex CNV 16pdel gene cohort, encourages further evaluation of *FAM57B* in brain development and function.

Correlating the multitude of symptoms to specific genes associated with a multigenic copy number variant region is extremely challenging. Variation in clinical phenotypes of 16p11.2 deletion syndrome patients further indicates the need to understand the biology of this CNV (Fetit et al., 2020). Previously, we identified gene interactions among the 16p11.2 interval (McCammon et al., 2017) that do not converge on functional networks predicted by ASD gene-set enrichment analysis by Pinto *et al.* (Pinto et al., 2010), suggesting indirect mechanisms of genetic interaction. We investigated the interaction between *doc2a*, encoding for a synaptic vesicle-associated calcium-binding protein, and *fam57ba*. Haploinsufficiency of this genetic interaction identified both a body and central nervous system phenotype, including seizure activity. No evidence for physical interactions between proteins encoded by 16p11.2 genes has been found (Lin et al., 2015). Along with *DOC2A*, several genes within the interval are candidate contributors to neurodevelopment and neuropsychiatric phenotypes, including *KCTD13, SEZ6L2, KIF22, MVP, TAOK2* and *QPRT*. In a functional screen, we defined genetic interaction between *fam57ba, kctd13, sez6l2* and *kif22* (McCammon et al., 2017). *KCTD13 encodes a ubiquitin ligase adaptor with cognitive defects identified in mice heterozygous for the gene*

(Chen et al., 2009, Golzio et al., 2012, Martin Lorenzo et al., 2021). KIF22 is a kinesin-like protein necessary for embryonic chromosome segregation and axonal branching patterns (Park et al., 2016, Antonio et al., 2000, Ohsugi et al., 2008). SEZ6L2 has been connected to seizure activity and modulates neurite outgrowth (Boonen et al., 2016). MVP can function as a regulator of the homeostatic component of experience-dependent behavior (Ip et al., 2018). *TAOK2* encodes a serine/threonine kinase that can play a role in dendrite formation (de Anda et al., 2012). *QPRT* encodes quinolinate phosphoribosyltransferase that catabolizes quinolinic acid, whose elevation has been linked to epilepsy and has also showed regulation by ASD candidate genes (Chiocchetti et al., 2016, Haslinger et al., 2018). The strong genetic interaction between *FAM57B* and most of the above-described genes highlights the connection between lipid regulation and brain development or maturation. Although *FAM57B* haploinsufficiency alone cannot account for the multitude of disrupted biochemical and cellular properties in 16pdel affected neurons, disrupted lipid metabolism is tightly correlated to 16pdel Syndrome. The insight into lipid alterations and a potential role for *FAM57B* in mediating these changes, gives a new view of mechanisms underlying 16pdel Syndrome, and holds promise for new therapeutic directions.

Limitations of the Study

In the large 16p11.2 copy number variant interval, haploinsufficient symptoms do not resolve to a single causal gene. *FAM57B* interacts genetically with many other 16p11.2 interval genes and is a strong candidate for contribution to symptomatology. We studied the poorly defined function of FAM57B to understand its role in lipid regulation and function in the brain. *FAM57B* mutant neuronal lines do not recapitulate all phenotypes associated with 16p11.2 deletion syndrome neurons. For instance, the *FAM57B* heterozygote SH-SY5Y differentiated neurons and zebrafish brains do not show exactly the same lipid profiles as neurons derived from 16p11.2 deletion iPSC, although there is overlap. Since 16pdel syndrome results from changes in gene dosage through haploinsufficiency, rescue of FAM57B levels must be precise to match endogenous levels to avoid spurious gene dosage effects. However, in the 16p11.2 chromosomal deletion, the *FAM57B* promoter and enhancer regions are also deleted, it is not an easy task to rescue FAM57B expression to endogenous levels. The nature of the copy number variant phenotype indicates that exogenous expression to rescue FAM57B could result in outcomes modulated by dosage, and that the entire gene with its regulatory regions would have to be used for rescue. The *FAM57B* regulatory regions have not been mapped, and so are not available for rescue constructs.

Acknowledgements

We thank Olivier Paugois for excellent fish care and lab management. Special thank you to the Whitehead Institute core facilities as follows: Wendy Salmon (Keck Imaging Facility) for help with confocal imaging, Eric Spooner (MS Core) for proteomic work, Dr. Caroline Lewis (Metabolomics Core) for lipidomics analysis, Dr. George Bell (Bioinformatics and Research Computing) for analysis and help in compiling MS/MS data and Dr.

Heather Keys (Functional Genomics Platform) for aid in CRISPR-induced *FAM57B* mutations. We thank Dr. Shifra Ben-Dor, Bioinformatics Unit, Life Sciences Core Facilities, Weizmann Institute of Science, for sequence alignment in Supplemental Fig 3. We thank Dr. Mike Gallagher for help analyzing the published FAM57B mutation from Satterstrom *et al.* 2019 (Satterstrom et al., 2019), Dr. Monika Saxena for constructive and helpful edits to the manuscript, Master of Science student Adrianna Vandeuren for help maintaining the fish lines, and Undergraduate Research Opportunity student Allysa Allen for help in expanding iPSCs. Finally, we would like to thank colleagues at the Simons Center for the Social Brain at MIT for collegial interactions. This work was supported by a grant from the Simons Foundation to the Simons Center for the Social Brain at MIT, National Institute of Mental Health (NIMH) of the National Institutes of Health (1R01MH119173-01A1), a Balkin-Weinberg-Markell Fellowship, the Israel Science Foundation Grant #3172/19 and additional support from Jim and Pat Poitras. RJ was supported by NIMH grant 2R01MH104610-20.

Author Contributions

DLT and HS designed the study, interpreted results and wrote the manuscript. AHF helped conceive, supervise, interpret and write the CerS study (**Fig. 3**). JK and YK performed the experiments in **Fig. 3**. JMM created the *fam57b mutant* zebrafish line. MM and RJ instructed on stem cell culture work and provided unaffected control iPSC (originally from Coriell Institute Biobank). DLT performed all other studies.

Declaration of Interests

The authors declared no potential conflicts of interest with respect to the research, authorship, and/or publication of this article.

STAR Methods

Resource Availability

Lead Contact

Further information and requests for resources and reagents should be directed to and will be fulfilled by the lead contact, Hazel Sive (h.sive@northeastern.edu).

Materials Availability

pcDNA3.1 FAM57B and CerS constructs, SH-SY5Y *FAM57B HET* and *FAM57B KO*, and Zebrafish lines *fam57ba*$^{+/-}$*;fam57bb*$^{+/-}$ and *fam57ba*$^{-/-}$*;fam57bb*$^{-/-}$ created in this manuscript are available upon request from lead contact.

Data Availability

- The authors declare that all data supporting the findings of this study are available within the article and its supplementary information.
- Raw data, including proteomics and lipidomics results, are available in the Supplemental Excel spreadsheet. Additional data can be requested from lead contact.
- Any additional information required to reanalyze the data reported in this paper is available from the lead contact upon request.

Experimental model and subject details

Animal Model

Adult zebrafish of the wildtype AB strain were maintained at 28˚C on 12h/12h light/dark cycle. Embryos were obtained from natural spawning and staged as previously described by Kimmel *et al.* (Kimmel et al., 1995). Due to the polygenic nature of sex determination and timing of gonadal development in zebrafish, we are unable to determine the sexes of the embryos and larvae for our assays. However, because our assays utilized large numbers of embryos and larvae, both sexes should be adequately represented. Embryos were obtained from separate crosses of *fam57b mut* mutant fish. *fam57b het* fish were generated by crossing *fam57b mut* to AB fish. The MIT Committee on Animal Care approved animal experimentation under protocol 0417-036-20. The Whitehead Institute Biosafety Committee approved of all materials under protocol HS001. All experiments conform to the relevant regulatory standards.

fam57ba$^{-/-}$ mutants were injected with *fam57bb* targeted sgRNA at 1 - 4 cell stage, previously described in McCammon *et al.* CRISPR/Cas9 induced mutation resulted in 17 bp deletion and early stop codon. Experiments were performed after 4 generations of crosses with AB controls.
fam57bb 5’ to 3’ TAGGTGATGTCCTGGCAGGAAG
fam57bb 3’ to 5’ AAACCTTCCTGCCAGGACATCA
For genotyping, PCR amplified region of in/del. PCR was digested with EarI restriction enzyme, with homozygous mutation detected by loss of EarI restriction site. *fam57b mut* line was outcrossed with AB periodically to avoid chromosomal abnormalities.

Generation and characterization of iPSC lines

Unaffected control male and female iPSC lines, 599 and 657, were a generous gift from Rudolf Jaenisch, originally obtained as fibroblasts from Coriell Institute Biobank. iPSC of 16p11.2 deletion carriers were obtained from Simons Variation in Individuals Project (Supplemental Table 1) (Simons Vip, 2012). Cell line corresponds to subjects with abbreviated ID from RUCDR. Acquisition of lines were in consideration of potential sex differences in 16pdel syndrome. All iPSCs were tested for negative mycoplasma and normal karyotype.

Cytogenetic analysis was performed on twenty G-banded metaphase cells at Cell Line Genetics. All experiments involving cells from human donors were performed in compliance with established IRB protocols at the Whitehead Institute. The Whitehead Institute for Biomedical Research and MIT Biosafety Committees approved safety considerations around the experiments performed.

iPSCs - Cells were cultured on plates coated with Matrigel (Corning #CB-40234A) in mTeSR+ media (STEMCELL Technologies #85850) with pen/strep. Y27632 (STEMCELL Tech #72302) was added to cells prior to passaging (single colonies), then passaged with ReLeSR or Accutase for single colonies (STEMCELL Technologies #05872 and #07922). Cells were maintained at 37°C with 5% O_2.

Generation of Cortical Neurons - iPSCs were differentiated into neural progenitor cells (NPCs) by FGF exchange. FGF was slowly removed by exchanging mTeSR+ with -FGF media (DMEM/F12/HEPES (Thermo Fisher Scientific #12400024), Neurobasal (Thermo Fisher Scientific #21103049), N2 (Gibco #17502048), Gem21 (GeminiBio #400-160) MEM non-essential amino acids (NEAA) (Thermo Fisher Scientific #11140050), GlutaMAX (Gibco #35050061), pen/strep, D(+) Glucose and NaCl) every day over 2 - 3 weeks. When rosettes were present, media was exchanged with +FGF media (DMEM/F12/HEPES, Neurobasal, N2, Gem21 - Vitamin A (GeminiBio #400161), MEM NEAA, GlutaMAX, pen/strep, Beta-Mercaptoethanol (Sigma-Aldrich #M3148) and 4 ng/mL FGF (Peprotech #100-18B)) plus 2.5 µM/mL dorsomorphin (Tocris #3093). Cells were incubated with Y27632 before passaging with Accutase, expanded and passaged at least 3 times until homogeneous NPC culture. NPCs were passaged on poly-D-lysine (Thermo Fisher Scientific #A3890401) and laminin (Sigma-Aldrich #L2020) coated plates for cortical neuron differentiation. NPCs media was exchanged with Neuronal Differentiation media (Neurobasal, GlutaMAX, NEAA, D(+) Glucose, Gem21, Culture One (Gibco #A3320201), 5 µg/mL BDNF and GDNF (Peprotech #450-02 & #450-10), pen/strep) for 1 month, changing media every 2 to 3 days. Cells were maintained at 37°C under normoxic conditions.

Generation and characterization of SH-SY5Y Neuroblastoma cell line

SH-SY5Y cells, originally from ATCC, were a kind gift from David Bartel, Whitehead Institute for Biomedical Research. Cells were maintained in EMEM (ATCC # 30-2003), F12 (ATCC # 30-2006) media supplemented with fetal bovine serum (FBS Sigma-Aldrich #12306C) and pen/strep in a 37˚C incubator with 5% CO_2. Differentiation of cells to neuronal model were induced with media containing Neurobasal, Gem21, GlutaMAX, All-trans-retinoic acid (Sigma-Aldrich # R2625) and pen/strep, for 4 days in dark to prevent retinoic acid degradation from light exposure (Kovalevich J, 2013).

CRISPR sgRNA designs were identified from Target Guide Sequence Cloning Protocol, Zhang lab, with sequence overlapping the TLC domain of FAM57B (Cong et al., 2013). 10 targeted guides to FAM57B sequence were individually transformed in pLC OPTI-Stuffer plasmid, a kind gift from David Sabatini,

Whitehead Institute, and lentivirus was grown in HEK293T cells. Generation of CRISPR/Cas9 induced mutations via lentiviral transduction was performed according to Wang *et al.* protocols (Wang et al., 2014, Wiles et al., 2015). After puromycin selection, cells were gently triturated and diluted to approximate 1 cell per well in 96 well plate. Wildtype cells were simultaneously single cell diluted and sorted to serve as additional control for experiments. Incorporation of mutation was determined by Next Generation Sequencing.

FAM57B Homozygote deletion (KO)
sgFAM57B1 5' to 3' - GGTGCTCCACCATGCCGCCA
Mutation resulted in frameshift with 111 and 121 bp deletion on either strand, resulting in early stop codon.

FAM57B Heterozygote deletion (HET)
sgFAM57B2 5' to 3' - GGGCACAGCAAATTGCGTGT
Mutation resulted in frameshift with 20 bp deletion on one strand, resulting in early stop codon.

Adeno-Associated Virus Integration Site 1 (AAVS1) targeted control
sgAAVS1 5' to 3' - CACCGGGGCCACTAGGGACAGGAT
Mutation resulted in frameshift and 51 bp and 1 bp deletion on either stand, resulting in early stop codon. The AAVS1 served as a control for all SH-SY5Y experiments. WT was compared to AAVS1 to determine confidence of statistical significance when compared to *FAM57B HET* and *KO*.

Method Details

HEK293 Cell Culture and Co-Immunoprecipitation

HEK293T cells were cultured in Dulbecco's modified Eagle's medium (Corning # MT15017CV) supplemented with 10% fetal bovine serum, 100 IU/ml penicillin, 100 µg/ml streptomycin, and 110 µg/ml sodium pyruvate. Transfections were performed with the polyethylenimine reagent (Sigma-Aldrich # 08719) using 8 µg of plasmid per 10 cm culture dish for 36–48 h; medium was exchanged after 6 hours. pcDNA3.1 was used as a control. DYKDDDDK (Flag)-tagged human FAM57B plasmid (sequence sent to Genscript and available upon request). Hemagglutinin (HA)-tagged human CerS plasmids were generated as described (Laviad et al., 2012).

Co-immunoprecipitation was performed using cells transfected with a variety of plasmids in pcDNA3.1-C-DYK or pcDNA3.1-C-HA (sequences sent to Genscript and available upon request). HA-tagged CerSs were used to confirm non-specific binding to Flag affinity resins. Cells were washed twice with cold PBS and lysed in lysis buffer (20 mM Tris (pH 7.4), 150 mM NaCl, 1 mM EDTA, 1% NP-40, 5% glycerol and protease inhibitor (Sigma-Aldrich #200-664-3)). Lysates were incubated on ice for 10-15 min. Protein was determined using the BCA reagent. FLAG-tagged human FAM57B, using an anti-FLAG affinity resin (Genscript #L00432). Lysates

were incubated with 40 µl of beads overnight at 4°C with rotation. The resin was washed three times in 1 ml of lysis buffer at 4°C with rotation. Proteins were eluted using 4X SDS sample buffer (BioRad #161-0747). Eluted proteins were analyzed by Western blotting for detection of HA-tagged interacting proteins.

Ceramide Synthase Assays

Cell homogenates were prepared in 20 mM HEPES-KOH, pH 7.2, 25 mM KCl, 250 mM sucrose, and 2 mM MgCl2 containing a protease inhibitor mixture. Protein was determined using the BCA reagent (Thermo Fisher Scientific). Samples were incubated with 15 µM NBD-sphinganine (Avanti Polar Lipids # 810206P), 20 µM defatted BSA (Sigma-Aldrich #10775835001), and 50 µM 16- or 24-fatty acyl-CoA (Avanti Polar Lipids 870743 & 870725) in a 20 µl reaction volume. CerS (40 µg protein, 25 min reaction time) was assayed using C24.1-CoA and Cer5/6 (5 µg protein, 5 min reaction time) assayed using C16-CoA. Reactions were terminated by chloroform/methanol (1:2, v/v) and lipids extracted. Lipids were dried under N2, resuspended in chloroform/methanol (9:1, v/v), and separated by thin layer chromatography using chloroform/methanol, 2M NH4OH (40:10:1, v/v/v) as the developing solvent. NBD-labeled lipids were visualized using an Amersham Typhoon5 imager and quantified by ImageQuantTL (GE Healthcare, Chalfont St Giles, UK). All solvents were of analytical grade and were purchased from Bio-Lab (Jerusalem, Israel).

Sample Collection for Lipidomics

iPSC Differentiated Neurons - 2 x 10^6 NPCs were plated in 6 well plate, at least 3 wells per genotype. Differentiation to cortical neurons was performed as stated above. Cells were washed with phosphate buffered saline solution (PBS). Cells were scraped in LC grade methanol and homogenized in eppendorf tube containing water and LC grade chloroform with pestle mixer, followed by vortexing for 10 minutes at 4°C. Lipids were separated by centrifuging top speed at 4°C. This was repeated three times with all samples run together in positive ion mode for lipidomic analysis. Raw data are provided in the Supplemental Excel spreadsheet.

Differentiated SH-SY5Y Cells - 1 x 10^6 cells were plated per well in 6 well plate, 3 wells per genotype. SH cells were differentiated over 4 days in media containing retinoic acid. Cells were washed with PBS. Cells were scraped in LC grade methanol and homogenized in eppendorf tube containing water and LC grade chloroform with pestle mixer, followed by vortexing for 10 minutes at 4°C. Lipids were separated by centrifuging top speed at 4°C. This was repeated twice with all samples run together. Raw data are provided in the Supplemental Excel spreadsheet.

Zebrafish - At 7 dpf, larvae were deeply anesthetized with tricaine. Brains with surrounding epidermal layer were dissected and flash frozen on dry ice. Collections were pooled at 20 brains per sample. Brains were homogenized in an eppendorf tube with a pestle mixer in LC grade methanol, LC grade chloroform and water, followed by vortexing for 10 minutes at 4°C. Lipids were separated by centrifuging top speed at 4°C. Brains

were collected and stored in -80°C over many dissections to acquire adequate tissue for analysis. This was repeated twice per genotype, with the *fam57b mut* and AB cohort run at different times (different normalization) while the *fam57b het* and AB cohort were run at the same time. Raw data are provided in the Supplemental Excel spreadsheet.

Untargeted Lipidomics

Lipids were separated on an Ascentis Express C18 2.1 x 150 mm 2.7 um column (Sigma-Aldrich) connected to a Vanquish Horizon UPLC system and an ID-X tribrid mass spectrometer (Thermo Fisher Scientific) equipped with a heated electrospray ionization (HESI) probe. External mass calibration was performed using the standard calibration mixture every seven days. Dried lipid extracts were reconstituted in 50 uL 65:30:5 acetonitrile: isopropanol: water (v/v/v). Typically, 2 uL of sample were injected onto the column, with separate injections for positive and negative ionization modes. Mobile phase A in the chromatographic method consisted of 60:40 water: acetonitrile with 10 mM ammonium formate and 0.1% formic acid, and mobile phase B consisted of 90:10 isopropanol: acetonitrile, with 10 mM ammonium formate and 0.1% formic acid. The chromatographic gradient was adapted from Hu *et al.* 2008 (Hu et al., 2008) and Bird *et al.* 2011 (Bird et al., 2011). Briefly, the elution was performed with a gradient of 40 min; during 0−1.5 min isocratic elution with 32% B; from 1.5 to 4 min increase to 45% B, from 4 to 5 min increase to 52% B, from 5 to 8 min to 58% B, from 8 to 11 min to 66% B, from 11 to 14 min to 70% B, from 14 to 18 min to 75% B, from 18 to 21 min to 97% B, during 21 to 35 min 97% B is maintained; from 35−35.1 min solvent B was decreased to 32% and then maintained for another 4.9 min for column re-equilibration. The flow rate was set to 0.260 mL/min. The column oven and autosampler were held at 55°C and 15°C, respectively. The mass spectrometer parameters were as follows: The spray voltage was set to 3.25 kV in positive mode and 3.0 kV in negative mode, and the heated capillary and the HESI were held at 300°C and 375°C, respectively. The S-lens RF level was set to 45, and the sheath and auxiliary gas were set to 40 and 10 units, respectively. These conditions were held constant for both positive and negative ionization mode acquisitions. The mass spectrometer was operated in full-scan-ddMS/MS mode with an orbitrap resolution of 120,000 (MS1) and 30,000 (MS/MS). Internal calibration using Easy IC was enabled. Quadrupole isolation was enabled, the AGC target was $1x10^5$, the maximum injection time was 50 msec, and the scan range was m/z = 200-2000. For data-dependent MS/MS, the cycle time as 1.5 sec, the isolation window was 1, and an intensity threshold of $1x10^3$ was used. HCD fragmentation was achieved using a step-wise collision energy of 15, 25, and 35 units, and detected in the orbitrap with an AGC target of $5x10^4$ and a maximum injection time of 54 msec. Isotopic exclusion was on, a dynamic exclusion window of 2.5 sec was used, and an exclusion list was generated using a solvent bank.

High-throughput annotation and relative quantification of lipids was performed using LipidSearch v4.2.21 (Thermo Fisher Scientific/ Mitsui Knowledge Industries) using the HCD database (Taguchi and Ishikawa, 2010, Yamada et al., 2013). LipidSearch matches MS/MS data in the experimental data with spectral data in the

HCD database. Precursor ion tolerance was set to 5 ppm, product ion tolerance was set to 10 ppm. LipidSearch nomenclature uses underscores to separate the fatty acyl chains to indicate the lack of *sn* positional information. In cases where there is insufficient MS/MS data to identify all acyl chains, only the sum of the chains is displayed. Following the peak search, positive and negative mode data were aligned together where possible and raw peak areas for all annotated lipids were exported to Microsoft Excel and filtered according to the following predetermined quality control criteria: Rej ("Reject" parameter calculated by LipidSearch) equal to 0; PQ ("Peak Quality" parameter calculated by LipidSearch software) greater than 0.75; CV (standard deviation/ mean peak area across triplicate injections of a represented (pooled) biological sample) below 0.4; R (linear correlation across a three-point dilution series of the representative (pooled) biological sample) greater than 0.9. Typically, ~70% of annotated lipids passed all four quality control criteria. Redundant lipid ions (those with identical retention times and multiple adducts) were removed such that only one lipid ion per species/ per unique retention time is reported in merged alignments. For data where positive and negative mode data were aligned separately some redundancies may still exist. Raw peak areas of the filtered lipids were normalized to total lipid signal (positive or negative ionization mode) in each sample to control for sample loading. Data presented are shown as Log_2FC compared to wildtype/control samples. Statistics were performed in Prism, with each run analyzed separately.

Zebrafish brain staining and imaging

For 24 hours post-fertilization staining, embryos were deeply anesthetized in tricaine after being dechorionated. Embryos were places into wells in 1% Agarose dishes. 1 ng Cholera Toxin subunit B (CT-B) (Recombinant Alexa Fluor 488 conjugate, Invitrogen #C34775) was injected into the hindbrain ventricle (Gutzman and Sive, 2010). Embryos were washed with E3 and incubated for 1 hour to allow CT-B binding. Embryos were then fixed in fresh 4% PFA in phosphate buffered solution (PBS) overnight at 4°C. Embryos were washed in PBS + Tween-20 (PBT) and incubated with 555-Phalloidin (Invitrogen #A34055) for 1 hour. Alternatively, embryos were incubated with Duramycin-Cy3 conjugate (Molecular Targeting Technologies #D-1006) PE stain for 45 min. Embryos were washed in PBT and mounted in DAPI Antifade (Thermo Fisher Scientific #P36931) overnight. Imaging was performed on an inverted Zeiss LSM700 Laser Scanning Confocal and processed on Fiji (ImageJ). CT-B and Duramycin images were processed on ImageJ to measure relative puncta from staining. Particles were measured after drawing a size circle in each hemisphere comparing AB to *fam57b mut* embryos. Threshold was set to intermodes to assume for bimodal histogram, particle size set between 0 – 2 μm^2.

For 7 dpf larvae, the following protocol was adapted from the mouse protocol provided by LifeCanvas Technologies (SHIELD kit, LifeCanvas Technologies). At 7 dpf, zebrafish were collected into Eppendorf tubes, 25 zebrafish per tube and anesthetized on ice briefly. Embryo buffer E3 was removed and replaced with 1 mL SHIELD Perfusion Solution with diluted 4% paraformaldehyde (PFA) (Electron Microscopy Sciences # 50-980-

495), shaking overnight at 4°C. Whole zebrafish brains were dissected the next day and placed into tubes with fresh SHIELD Perfusion Solution, shaking overnight at 4°C. Tissue was placed into 1 mL SHIELD OFF solution, shaking overnight at 4°C. Tissue was transferred into SHIELD ON Buffer, shaking overnight at 37°C in MaxQ 4450 (ThermoFisher Scientific). Tissue was then cleared with 1 mL passive clearing protocol using SDS Clearing Solution, shaking for 5 days at 45°C. Clearing solution was washed off with 1 mL PBS + 1% Triton-X (PBT) with 0.02% Sodium Azide 3 times over 24 hours shaking at 37°C. Tissue was blocked in 1 mL PBT + 1% BSA for 2 hours shaking at room temperature, then incubated in primary antibody, shaking overnight at 4°C. Antibodies: 1:100 Synaptotagmin-1 (Lifespan Bioscience # LS-B12889), GAD65 + GAD67 (Abcam #ab11070), Beta-Actin (Proteintech 60008-1) and 1:500 DAPI (Life Technologies # D1306), in 0.5 mL PBT + 1% BSA. Primary antibody was washed off 3 times in PBT and incubated in secondary antibody shaking overnight at 4 °C (1:500 488- 555- 680-conjugated antibodies (Jackson ImmunoResearch, 488 anti-goat #805-545-180, 488 anti-mouse #715-545-151, 594 anti-mouse #715-585-150, 594 anti-rabbit #711-585-152, anti-mouse 680 #715-625-150, anti-rabbit 680 #711-625-152) in PBT + 1% BSA). Secondary was washed off 3 times in PBT, then 1 mL EasyIndex was added to tissue, shaking overnight at room temperature. Whole brains were mounted in fresh EasyIndex on slides, placing coverslip with vacuum grease. Imaging was performed on an inverted Zeiss LSM700 Laser Scanning Confocal and processed on Fiji (ImageJ).

PH3 Staining

At 24 hpf, *fam57b mut* and AB embryos were dechorionated and fixed overnight at 4°C in paraformaldehyde. Embryos were washed with phosphate buffered saline with Tween-20 (PBT) and yolk sac was removed. Embryos were incubated with 10% H_2O_2 for 1.5 hrs, then washed in PBT. Embryos were blocked in PBT with bovine serum albumin at room temp for 4 hrs, then incubated with α-PH3 antibody (1:1000, Upstate Biotechnology #06-570) overnight at room temp. Embryos were washed with PBT and incubated with secondary antibody (1:500 goat α-rabbit IgG HRP, Invitrogen #31460) in PBT overnight at room temp. Embryos were washed in PBT and flat mounted on glass slide with propidium iodide in glycerol. Imaging was performed on a confocal microscope.

TUNEL Staining

Embryos were collected, fixed and processed as PH3 staining. Embryos were then dehydrated then rehydrated interchanging ethanol and PBT. Proteinase K (Invitrogen # EO0491) was incubated in PBT on neutator, then rinsed in PBT. TdT labeling was followed per manufacturer's instructions, ApopTag kit (Chemicon # S7101). α-DIG (1:100, Thermo Fisher Scientific #700772) was used to detect the DIG labeled ends. Embryos were washed in PBT and flat mounted on glass slide with propidium iodide in glycerol. Imaging was performed on a confocal microscope.

Immunocytochemistry

Patient derived neurons were washed with PBS and fixed in fresh 4% paraformaldehyde in PBS overnight rocking at 4°C. Cells were washed with PBT and blocked in PBT + BSA for 1 hour at room temperature. Primary antibody was added to PBT overnight rocking at 4°C. Antibodies: 1:100 Syt-1, Vesicular Glutamate 1 and 2 (VGlut1/2, Synaptic Systems #135503) or Postsynaptic Density 95 (PSD95, Abcam #ab18258), Acetylated-Tubulin (Ac-Tubulin, Abcam #ab179513). Primary antibody was washed off 3 times in PBT and incubated in secondary antibody shaking overnight at 4°C (1:500 488- 555- 680- (Jackson ImmunoResearch, see above) in PBT + BSA). Secondary was washed off 3 times in PBT, rocking for 2 hours at room temperature. Cells were washed 3 times in PBT and mounted on slides with DAPI (Prolong Gold Antifade with DAPI (Life Technologies #P36935). Imaging was performed on an inverted Zeiss LSM700 Laser Scanning Confocal and processed on Fiji (ImageJ).

SH-SY5Y cells were plated on coverslips and differentiated over 4 days with retinoic acid medium. The same imaging protocol was performed as above. Antibody: 1:200 Beta-Actin.

Western blot

HEK293T studies - Proteins were separated by SDS-PAGE and transferred to nitrocellulose membranes. HA-tagged constructs were identified using antibodies against HA or Flag peptides (1:5,000, Abcam #ab18181, #ab1162), and goat anti-rabbit or mouse horseradish peroxidase (1:10,000, #323-001-021, #223-005-024) were used as secondary antibodies (Jackson). Equal loading was confirmed using a mouse anti-GAPDH (Abcam #ab8245). Detection was performed using the ECL detection system.

Larvae brain tissue (25 larvae brains pooled per sample) or differentiated SH-SY5Y cells (1 x 10^6 cells per sample) were washed with PBS then lysed in RIPA buffer (Thermo Fisher Scientific #89900) with protease inhibitor cocktail with a pestle homogenizer. Tissue/cells were rotate at 4°C for 30 min, then spun full speed 10 min. The supernatant was removed containing proteins, with denature in laemmli buffer for 1 hr at RT. Protein was separated on 10-40% gel and transferred PVDF by wet transfer. Membranes were blocked in 5% dry milk in TBS + Tween 20. Primary antibody was incubated overnight. Same antibodies were used for immunofluorescence and western analysis. Antibodies: Syt-1, Beta-Actin, GAPDH), FAM57B (Proteintech 20760-1-AP). Secondary antibodies 1:2000 IRDye (Li-Cor 800CW Rabbit #92632211, 680RD Mouse #92668070) were incubated for 1 hour at room temperature. Blots were imaged and quantified on a Li-Cor Odyssey.

Biotinylation and MS/MS

At 7 dpf, larvae were deeply anesthetized with tricaine. Larvae were dissected in PBS with protease inhibitor cocktail on ice, pooling 20 brains per genotype per sample. Assay was performed according to protocol utilizing Pierce Cell Surface Protein Isolation Kit (Thermo Fisher Scientific #89881) with the following

modifications. 1 vial of biotin was resuspended in 2 mL PBS and fresh brains were incubated with 1 mL biotin/PBS solution rotating for 45 minutes at 4C. Elution of biotin-bound proteins in water + DTT 1 hour at room temperature. Eluates were reduced, alkylated and digested with trypsin at 37°C overnight. This solution was subjected to solid phase extraction to concentrate the peptides and remove unwanted reagents. Solution was injected onto a Waters NanoAcquity HPLC equipped with a self-packed Aeris 3.6 µm C18 analytical column 0.075 mm by 20 cm, (Phenomenex). Peptides were eluted using standard reverse-phase gradients. The effluent from the column was analyzed using a Thermo Orbitrap Elite mass spectrometer (nanospray configuration) operated in a data dependent manner for 54 minutes. The resulting fragmentation spectra were correlated against the known database using Mascot (Matrix Science). Scaffold Q+S (Proteome Software) was used to provide consensus reports for the identified proteins. PEAKS Studio 8.5 was used for data analysis as a supplement to Mascot. Raw data are provided in the Supplemental Excel spreadsheet.

Synaptosome Isolation

7 dpf zebrafish larvae were anesthetized in Tricaine with larvae buffer E3. Whole brains were dissected from the larvae and placed into a 1.5 mL Eppendorf tube on ice, pooling 20 brains per genotype. The tissue was centrifuged at top speed and excess liquid was removed. 200 µl of SYN-Per Reagent (Thermo Fisher Scientific #87793) plus protease cocktail inhibitor was added to the eppendorf on ice. With a pestle, the brains were homogenized with 10 strokes and the tube was gently turned 3 times to dissociate cells. The tissue was centrifuged at 1200 x G for 10 min at 4°C. The supernatant was collected and added to a new Eppendorf tube. The sample was centrifuged at 15,000 x G for 20 min at 4°C. The supernatant was removed and the pellet was gently resuspended in 100 µl of SYN-Per Reagent plus protease cocktail inhibitor. The samples were flash frozen and processed for tandem mass spectrometry (MS/MS) after reducing alkylating and digesting with trypsin as indicated above.

SH-SY5Y cells were plated at 1 x 10^6 per well in 6 well plates, with 1 well per independent sample for all genotypes. After 4 days differentiation, cells were washed with PBS plus protease inhibitor cocktail. Cells were scraped in the same solution and centrifuges in 1.5 mL Eppendorf tube at top speed for 30 seconds at 4°C. The wash was removed and the same protocol was used as for larval brain synaptosome isolation. After samples were flash frozen, they were then processed for MS/MS or LC/MS analysis. Raw data are provided in the Supplemental Excel spreadsheet.

Electrophysiology

iPSC Differentiated Neurons - 1 x 10^4 NPCs were plated and matured over 1 month in a PDL and Laminin coated 48-well CytoView plate (Axion Biosystems # M768-tMEA-48B). Recordings of spontaneous activity were taken over 10-minute periods on the Maestro system (Axion Biosystems). AxIS software compiled the data collected from recordings. Data were collected for LFPs (firing frequency in Hz), electrographic burst

events (minimum 5 LFPs/100 ms) and relative network activity (minimum 3 LFPs detected simultaneously between a minimum of two electrodes). LFP detection was filtered at 6 × standard deviation to remove potential artifacts. The external physiological solution contained (in mM) 128 NaCl, 5 KCl, 2 $CaCl_2$, 1 $MgCl_2$, 25 HEPES and 30 glucose, pH 7.3, Osmolarity 315 - 325. The High KCl solution contained (in mM) 63 NaCl, 70 KCl, 2 $CaCl_2$, 1 $MgCl_2$, 25 HEPES and 30 glucose, pH 7.3, Osmolarity 315 - 325.

Live larvae MEA recordings were performed as detailed in Tomasello and Sive 2020 (Tomasello and Sive, 2020). For these recordings, larva was immersed in low-melt agarose in 12-well 64 electrode Cytoview plates (Axion Biosystems (discontinued, recommend 6-well plate)). LFP activity was recorded for 10 minutes, noting the electrodes in contact with larva head region. Larva were immediately sacrificed after recordings. Data was processed with AxIS and Axion Neural Metric Tool (Axion Biosystems).

Larval Behavior

At 7 dpf, dishes containing larvae were moved to the bench to allow acclimation to RT. For experimentation, only larvae with an inflated swim bladder and no other morphology phenotypes, such as a crooked tail, were selected. With a cut 200 µl tip, larvae were individually pipetted into 96-well plates with 200 µl E3 media and moved to the Noldus Daniovision for 10 min habituation period. The larvae were exposed to a testing period of 70 minutes, with light (at 10%) extinguished for 5 seconds at 10-minute intervals. Point tracking collected distance and velocity traveled. Distance moved was calculated using the Ethovision XT 11 software from Noldus. Raw data are provided in the Supplemental Excel spreadsheet.

The same method is performed as above up to habituation. Baseline activity was then recorded for 10 minutes, followed by exchange of 100 µl E3 from each well with 100 µl of varying concentrations of PTZ to test a range of doses. Plates were immediately placed back on the Daniovision system for another 10 min recording. Point tracking collected distance and velocity traveled. Distance moved was calculated using the Ethovision XT 11 software from Noldus, normalizing to habituation time. Raw data are provided in the Supplemental Excel spreadsheet.

Neuromuscular Junction Staining

Larvae were fixed in 4% PFA. Alpha-Bungarotoxin AlexaFluor 488 conjugate (Invitrogen B13422) was used at 1:500, znp1 (anti-SYT2, Abcam ab154035) monoclonal antibody was used at 1:200, with secondary antibody 594 anti-mouse (Jackson #715-585-150) incubated at 1:500.

Larval Head Measurements

Larvae were deeply anesthetized in tricaine and immersed in methylcellulose for brightfield imaging on Leica microscope. Larvae were oriented for dorsal measurements of dorsal head length, hindbrain head length, inter-

eye width and forebrain head length, and oriented for lateral measurements of head height, lateral head length, eye width, eye height and lateral length. Schematic of measurements can be found in McCammon *et al.* 2017 (McCammon et al., 2017). Raw data and conversion measurements are provided in the Supplemental Excel spreadsheet.

Quantification and statistical analysis

With exception to proteomic analysis in Figures 5C, 5D, 7E, 7H, all statistical analysis was performed in Prism. Statistical test is denoted in the figure legend corresponding to the appropriate figure. Error bars represent standard error of the mean. Asterisks are defined in each relevant figure legend. On the lipidomic analysis of individual species, to correct p-values we had utilized Sidak's multiple comparisons post hoc test rather than FDR. Note, we tried FDR for multiple hypothesis correction, and that method produced similar results. GO SLIM analysis was performed with PANTHER Classification System (www.pantherdb.org) that combines genomes, gene function classifications, pathways and statistical analysis tools to enable biologists to analyze large-scale genome-wide experimental data (Mi et al., 2019). For the Proteomics analysis, the peptide intensities of biological samples were analyzed with MSstats, an R package for statistical analysis, using the options FDR=0.05 or 0.01, 'removeProtein_with1Feature=TRUE' and 'fewMeasurements="remove"'. The labeled genes indicate lowest p-values. For post hoc colocalization analysis of iPSC differentiated neurons (Table 2), individual cell somas were outlined by freehand in FIJI, followed by Coloc 2 colocalization analysis between Synaptotagmin-1 (Channel 1) and PSD-95 (Channel 2). Neurons were isolated between 3 images per genotype of representative images from Supplemental Fig. 1. Similar statistics are indicated between control 16pdel neurons.

Additional Resources

REAGENT or RESOURCE	SOURCE	IDENTIFIER
Antibodies		
Synaptotagmin-1	Lifespan Bioscience	LS-B12889
GAD65 + 67	Abcam	ab11070
Beta-Actin	Proteintech	60008-1
DAPI	Life Technologies	D1306
555-Phalloidin	Invitrogen	A34055
488 anti-goat	Jackson	805-545-180,
488 anti-mouse	Jackson	715-545-151
594 anti-mouse	Jackson	715-585-150
594 anti-rabbit	Jackson	711-585-152
anti-mouse 680	Jackson	715-625-150
anti-rabbit 680	Jackson	711-625-152
VGlut1/2	Synaptic Systems	135503
PSD95	Abcam	ab18258
Ac-Tubulin	Abcam	ab179513
Prolong Gold Antifade with DAPI	LifeTech	P36935
HA	Abcam	ab18181

FLAG	Abcam	ab1162
GAPDH	Abcam	ab8245
Li-Cor 800CW Rabbit	Li-Cor	92632211
Li-Cor 680RD Mouse	Li-Cor	92668070
Chemicals, peptides, and recombinant proteins		
Matrigel	Corning	CB-40234A
mTeSR+	STEMCELL Tech	85850
Y27632	STEMCELL Tech	72302
ReLeSR	STEMCELL Tech	05872
Accutase	STEMCELL Tech	07922
DMEM/F12/HEPES	Thermo	12400024
Neurobasal	Thermo	21103049
N2	Gibco	17502048
Gem21	GeminiBio	400-160
MEM NEAA	Thermo	11140050
GlutaMAX	Gibco	35050061
Gem21 - Vit A	GeminiBio	400161
Beta-Mercaptoethanol	Sigma	M3148
FGF	Peprotech	100-18B
BDNF	Peprotech	450-02
GDNF	Peprotech	450-10
Dorsomorphin	Tocis	3093
Poly-D-Lysine	Thermo	A3890401
Laminin	Sigma	L2020
EMEM	ATCC	30-2003
F12	ATCC	30-2006
FBS	Sigma	12306C
All-trans-RA	Sigma	R2625
DMEM	Corning	MT15017CV
Polyethylenimine	Sigma	08719
Protease Inhibitor Cocktail	Sigma	200-664-3
NBD-spinganine	Avanti Polar	810206P
BSA -FA	Sigma	10775835001
16.1 Coenzyme A	Avanti Polar	870743
24.1 Coenzyme 1	Avanti Polar	870725
CT-B	Invitrogen	C34775
Duramycin-Cy3	Molecular Targeting	D-1006
SHIELD	LifeCanvas Tech	https://lifecanvastech.com/products/shield
PFA	EMS	50-970-495
RIPA	Thermo	89900
SYN-Per	Thermo	87793
Critical commercial assays		
Pierce Cell Surface Protein Isolation Kit	Thermo	89881
Deposited data		
Lipidomics	This Paper	Supplemental Excel
Biotinylation Proteomics	This Paper	Supplemental Excel
Synaptosome Proteomics	This Paper	Supplemental Excel
Experimental models: Cell lines		
SH-SY5Y	ATCC	CRL-2266
HEK293T	ATCC	CRL-3216

IPSC 16pdel 1453	Simons VIP	SV0001453
IPSC 16pdel 1455	Simons VIP	SV0001455
IPSC 16pdel 1459	Simons VIP	SV0001459
IPSC 16pdel 1473	Simons VIP	SV0001473
IPSC 16pdel 1481	Simons VIP	SV0001481
IPSC 16pdel 1495	Simons VIP	SV0001495
IPSC 16pdel 3104	Simons VIP	SS0013104
IPSC CTR 599	Corriell Institute Biobank	AG07599
IPSC CTR 675	Corriell Institute Biobank	AG07657
Experimental models: Organisms/strains		
fam57ba$^{-/-}$;*fam57bb*$^{-/-}$ Zebrafish	This Paper	
FAM57B HET SH-SY5Y	This Paper	
FAM57B KO SH-SY5Y	This Paper	
FAM57B AAVS1 SH-SY5Y	This Paper	
Oligonucleotides		
fam57bb 5' to 3' TAGGTGATGTCCTGGCAGGAAG	This Paper	
fam57bb 3' to 5' AAACCTTCCTGCCAGGACATCA	This Paper	
sgFAM57B1 5' to 3' - GGTGCTCCACCATGCCGCCA	This Paper	
sgFAM57B2 5' to 3' - GGGCACAGCAAATTGCGTGT	This Paper	
sgAAVS1 5' to 3' - CACCGGGGCCACTAGGGACAGGAT	This Paper	
Recombinant DNA		
FAM57B-Flag	This Paper	
CerS2-HA	This Paper	
CerS5-HA	This Paper	
CerS6-HA	This Paper	
Software and algorithms		
AxIS and Neural Metric Tool	Axion Biosystems	Axionbiosystems.com
FIJI ImageJ	ImageJ	Imagej.net
GO SLIM analysis	PANTHER	pantherdb.org
LipidSearch	Thermo Scientific	IQLAAEGABSFAPCMBFK
Mascot	Matrix Science	Matrixscience.com
Scaffold Q+S	Proteome Software	Proteomesoftware.com
PEAKS Studio 8.5	Bioinformatics Solutions Inc.	Bioinfor.com
EthoVision XT	Noldus	Noldus.com

Main Figure Titles and Legends

Figure 1. Augmented local field potential activity in 16pdel syndrome differentiated neuronal culture. **a)** Local Field Potential (LFP) summary analyzed by log2 fold change between control and 16pdel patient differentiated neurons. MEA activity was recorded over 30 min starting in media, followed by physiological and high potassium chloride (KCl) solution. Data was summarized and pooled from 3 experiments. Control n = 9 (media), n = 17 (Physiological Solution), n = 13 (High KCl Solution). 16pdel n = 35 (media), n = 76

(Physiological Solution), n = 35 (High KCl Solution). Violin plot group analysis: Control - 16pdel 2-way ANOVA. *p ≤ 0.05. Technical experimental replicates n = 3.

b) Increased sex specific activity in female 16pdel probands drives overall increased LFPs, compared to unaffected controls. Media unaffected neurons (Control) male (♂) n = 3, Control female (♀) n = 6,16pdel neurons (Proband) ♂ n = 21, Proband ♀ n = 14, Physiological Solution Control ♂ n = 7, Control ♀ n = 10, Proband ♂ n = 38, Proband ♀ n = 38, High KCl Solution Control ♂ n = 6, Control ♀ n = 7, Proband ♂ n = 18, Proband ♀ n = 17. Violin plot analysis: male vs female T-Test. ****p ≤ 0.0001.

c) Increased sex specific female electrogenic burst frequency analyzed by log2 fold change between 16pdel male and female Media ♂ n = 21, ♀ n = 14, Physiological Solution ♂ n = 38, ♀ n = 38, High KCl Solution ♂ = 18, ♀ n = 17. Violin plot analysis: male vs female T-Test. *p ≤ 0.05. Technical experimental replicates n = 3.

Figure 2. Significant lipid changes between control and 16pdel differentiated neurons.

a) Total log2 fold change from normalized peak area of lipid class analysis from untargeted lipidomics. Bolded and colored indicate statistically significant changes by T-Test, p ≤ 0.05 - 0.0001.

AcCa acyl carnitine, AEA N-arachidonoylethanolamine, Cer ceramide, ChE cholesterol ester, Co coenzyme, DG diacylglycerol, Hex1Cer hexosylceramide, LPC lysophosphatiylcholine, LPE lysophosphatiylethanolamine, LPG lysophosphatiylglycerol, MG monoacylglycerol, PA phosphatidic acid, PC phosphatidylcholine, PE phosphatidylethanolamine, PG phosphatidylglycerol, PI phosphatidylinositol, PS phosphatidylserine, SM sphingomyelin, SPH sphingosine,TG triacylglycerol.

b) Total lipid composition analysis from untargeted lipidomics between control and 16pdel neuron. Chain Length: Small 1-5, Medium 6-12, Long 13-21, Very Long 22+, and Unresolved.

c – f) Selected analysis of lipid species from untargeted lipidomics classes. Lipid Class specified for each histogram (c - phosphatidylethanolamine, d - ceramide, e - monoacylglycerol, f – triacylglycerol) normalized peak area between control (grey) and 16pdel (orange). Statistical analysis by 2-Way ANOVA, *p ≤ 0.05 **p ≤ 0.01,***p ≤ 0.001, ****p ≤ 0.0001. Control n = 10, 16pdel n= 69, error bars represent SEM. TG and PE long and very long chain species not shown as no significant differences were found by ANOVA. Technical experimental replicates n = 3.

Figure 3. FAM57B interacts with CerS but does not have CerS activity.

a) CerS2 activity assayed using C24:1-CoA in *CerS2 KO* HEK293T cells. Statistical analysis by T-test *p ≤ 0.05, **p ≤ 0.01, error bars SEM. Technical experimental replicates n = 3.

b) (Upper) Western blot analysis of total human FAM57B-Flag and CerS2-HA after transfection in HEK293T cells. Proteins were prepared from HEK293T cells overexpressing the indicated constructs. Anti-HA and anti-Flag are indicated. (Lower) CerS2 activity assayed using C24:1-CoA in HEK293T cells. GAPDH was used as a loading control. Statistical analysis by T-test *p ≤ 0.05, **p ≤ 0.01, error bars SEM. Technical experimental replicates n = 3.

c) (Upper) Western blot analysis of total human FAM57B-Flag, CerS5-HA and CerS6-HA after transfection in HEK293T cells. Proteins were prepared from cells overexpressing the indicated constructs. Anti-HA and anti-Flag are indicated. (Lower) CerS5 and CerS6 activity was assayed using C16:0-CoA in HEK293T cells. Anti-HA and anti-Flag are indicated. GAPDH was used as a loading control. Technical experimental replicates n = 4.

d) Total cell lysates were prepared from the co-transfected cells with FAM57B-Flag and CerS2, 5 or 6-HA constructs and solubilized with 1% NP-40. Total lysates (input) or proteins immuno-precipitated with anti-Flag M2 agarose (IP) were subjected to immunoblotting with anti-HA or anti-Flag antibodies. GAPDH was used as a loading control. Technical experimental replicates n = 3.

Figure 4. Significant lipid changes in sphingolipids and glycerolipids between WT and *FAM57B mutant* human differentiated SH-SY5Y neuronal cells.

a - c) Total log2 fold change from normalized peak area of lipid class analysis from untargeted lipidomics. **a)** *FAM57B KO* – WT, **b)** *FAM57B HET* – WT, **c)** *FAM57B KO – FAM57B HET*. Bolded and colored indicate statistically significant changes by T-Test, p ≤ 0.05 - 0.0001. AcCa acyl carnitine, Cer ceramide, ChE cholesterol ester, CL cardiolipin, Co coenzyme, DG diacylglycerol, HexCer Hexosylceramide, LPC lysophosphatiylcholine, LPE lysophosphatiylethanolamine, MG monoacylglycerol, PC phosphatidylcholine, PE phosphatidylethanolamine, PG phosphatidylglycerol, PI phosphatidylinositol, PS phosphatidylserine, SM sphingomyelin, TG triacylglycerol. Technical experimental replicates n = 3.

d – g) Selected analysis of lipid species from untargeted lipidomics classes. Lipid Class specified for each histogram, normalized peak area between WT (black) *FAM57B HET* (orange) and *FAM57B KO* (blue). Statistical analysis by 2-Way ANOVA, *p ≤ 0.05 **p ≤ 0.01, ***p ≤ 0.001, ****p ≤ 0.0001. Color of asterisks indicate comparison between WT – HET (orange), WT – KO (blue), HET – KO (black). WT n = 3, *FAM57B HET* n= 3, *FAM57B KO* n = 3, error bars represent SEM. Experiment repeated twice, analysis was similar between two separate runs.

Figure 5. *FAM57B* knockout human neurons indicate altered synaptic composition.

a-b) Isolated synaptosome protein abundance changes between **a)** *FAM57B KO* relative to WT and **b)** *FAM57B HET* relative to WT (Log2 Fold). Labeled and colored indicating increased (purple) or decreased (green) abundance. Only the top 20 proteins of statical significance were labeled in **c** and analyzed in **e-g**. WT n = 8, HET n = 10, KO n = 7. Technical experimental replicates n = 3.

c-e) Gene ontology analysis of statistically significant synaptosome isolated proteins (e) in *FAM57B KO* relative to WT. **e)** gene ontology pie graphs of top 20 decreased protein groups of cellular components, molecular function, protein classes, biological processes and pathways. **f)** gene ontology figure legend.

g) Analysis of synaptic markers from isolated synaptosomes between all 3 genotypes. Bolded are significantly decreased protein abundance of synaptic structural and maturation proteins, and vesicle regulation machinery.

INA – WT - HET & WT - KO, RAB11B – HET - KO, STXBP1 – WT - HET & WT - KO, YWHAZ – WT - HET & WT - KO. 2-Way ANOVA, $p \leq 0.05$ – 0.0001.

f) Isolated synaptosome lipid abundance between *FAM57B KO* relative to WT. Bolded text and color (purple increased and green decreased) indicates statistically significant changes by T-Test, $p \leq 0.05$ - 0.01. n = 6 per genotype, technical experimental replicates n = 2. No statistically significant differences observed when comparing FAM57B HET to WT, nor *FAM57B KO* to *FAM57B HET*.

Figure 6. Significant lipid changes in ceramides and glycerols between AB and *fam57b mut* brain tissue.

a) Total log2 fold change from normalized peak area of lipid class analysis from untargeted lipidomics. Bolded and colored indicate statistically significant changes by T-Test, $p \leq 0.05$ - 0.0001. AcCa acyl carnitine, Cer ceramide, ChE cholesterol ester, CL cardiolipin, Co coenzyme, DG diacylglycerol, HexCer Hexosylceramide, LPC lysophosphatiylcholine, LPE lysophosphatiylethanolamine, MG monoacylglycerol, PC phosphatidylcholine, PE phosphatidylethanolamine, PG phosphatidylglycerol, PI phosphatidylinositol, PS phosphatidylserine, SM sphingomyelin, TG triacylglycerol. Technical experimental replicates n = 3.

b – g) Selected analysis of lipid species from untargeted lipidomics classes. Lipid Class specified for each histogram, normalized peak area between AB (grey) and *fam57b mut* (green). Statistical analysis by 2-Way ANOVA, *$p \leq 0.05$ **$p \leq 0.01$,***$p \leq 0.001$, ****$p \leq 0.0001$. AB n = 3, *fam57b mut* n= 3, error bars represent SEM. Experiment repeated twice, analysis was similar between two separate runs. Individual MG species between *fam57b het* to AB n.s. Not shown for space: 2-Way ANOVA analysis of TG. Increase in TG (16:0_16:0_16:1) in *fam57b het* compared to AB ($p \leq 0.01$).

Figure 7. Loss of *fam57b* results in altered plasma membrane architecture early in development and decreased localization of Synaptotagmin family at the synapse later in development.

a) Schematic of Cholera toxin-B-488 (CT-B) injection into hindbrain ventricle of embryo and flat-mounted midbrain region for imaging at 24 hpf.

b) Representative embryo midbrain imaging and quantification of CT-B labeling of AB compared to *fam57b mut*. Punctate CT-B labeling (arrows), actin marker phalloidin indicates labelling of CT-B at the plasma membrane, merged with DAPI. Quantification of puncta between WT (grey) and *fam57b mut* (green) CT-B ($p \leq 0.05$) T-Test. Scale bar = 5 μm. AB n = 16, *fam57b mut* n = 18. Error bars SEM, statistical analysis by T-test *$p \leq 0.05$. Technical experimental replicates n = 4.

c) Representative embryo midbrain imaging and quantification of duramycin-488 labeling of AB compared to *fam57b mut*. Punctate duramycin labeling (arrows), actin marker phalloidin indicates labelling of duramycin at the plasma membrane, merged with DAPI. Quantification of puncta between WT (grey) and *fam57b mut* (green) Duramycin PE staining ($p \leq 0.05$) T-Test. Scale bar = 5 μm. AB n = 8, *fam57b mut* n = 8. Error bars SEM, statistical analysis by T-test *$p \leq 0.05$. Technical experimental replicates n = 3.

d) Schematic of membrane protein labeling biotinylation assay and processing for MS/MS in 7 dpf larvae brains.

e) Larvae brain total plasma membrane protein abundance changes between *fam57b mut* relative to AB (Log2 Fold). Statistically significant p ≤ 0.05 - 0.0001 proteins labelled, indicating increased (purple) or decreased (green) abundance. Lowest abundance membrane protein Synaptotagmin-1a (red box). n = 3 per genotype.

f) Representative slice of 7 dpf whole larva brain mount with Sytaptotagmin-1a (green), GAD65/67 (red) and Beta-actin (magenta). Z-stack composite image merged with DAPI. Forebrain and midbrain areas of diffused Syt-1 localization (white arrows). Anatomical differences noted throughout brain, including (1) optic tectum and (2) corpus cerebelli (red arrows). Scale bar = 10 μm. Technical experimental replicates n = 2.

g) Representative 7 dpf whole brain western blot indicate no significant change in total Syt-1a protein levels between *fam57b mut* relative to AB. Zebrafish larvae brains pooled (20 per genotype). Syt-1a protein abundance normalized to Beta-Actin loading control, repeated twice.

h) Larvae brain total isolated synaptosome protein abundance changes between *fam57b mut* relative to AB (Log2 Fold). Statistically significant p ≤ 0.05 - 0.0001 proteins labelled, indicating increased (purple) or decreased (green) abundance. Low abundance Synaptotagmin-2a like protein (red box). n = 7 per genotype. Technical experimental replicates n = 2.

i-j) Gene ontology analysis of statistically significant larvae synaptosome isolated proteins (h) in *fam57b mut* relative to AB. i) Gene ontology pie graphs of increased and decreased protein groups of cellular components, molecular function, protein classes, biological processes and pathways. j) Gene ontology figure legend.

k) Analysis of Synaptotagmin family members from larvae isolated synaptosomes. Significantly decreased protein abundance of Syt1a and Syt2a by 2-Way ANOVA, **p ≤ 0.01, ****p ≤ 0.0001.

l) Analysis of Synaptotagmin family members from differentiated SH-SY5Y isolated synaptosomes between all 3 genotypes. Significantly decreased protein abundance of elongated ESYT1 by 2-Way ANOVA, *p ≤ 0.05, **p ≤ 0.01. Error bars SEM.

m) Analysis of synaptic markers from larvae isolated synaptosomes. Significantly decreased protein abundance (bolded) of vesicle regulation machinery and glutamate receptor activity by 2-Way ANOVA, **p ≤ 0.01, ****p ≤ 0.0001.

Figure 8. Decreased spontaneous brain activity and diminished behavioral response after stimuli presentation in *fam57b* mutants.

a-b) Local field potential (LFP) recordings in unanesthetized live larvae at 7dpf. Brain localized LFP recordings were pooled for each larva. **a)** Decreased average number, mean rate and inter-LFP interval (ILI) coefficient of variation of LFP in *fam57b mut* compared to AB (orange). No electrographic burst activity was identified in *fam57b mut* at standard 5 LFPs/100 ms. Decreased electrographic burst parameters, including duration, number of LFPs per burst, frequency and percentage at 3 LFPs/200ms (blue). **b)** Decreased average electrographic burst network activity and frequency, defined as a minimum or 3 electrographic bursts between

2 electrodes simultaneously, in *fam57b mut* compared to AB (grey). AB n = 21, *fam57b mut* n = 24 over 6 experiments. Statistical significance by unpaired T-test, *p ≤0.05, **p ≤ 0.01,*** p ≤ 0.001,**** p ≤ 0.0001. Technical experimental replicates n = 7.

c) Representative LFP waveform in brain region, indicating smaller relative waveform in *fam57b mut* compared to AB.

d) Representative LFP raster plot over experimental time frame, indicating less overall activity in *fam57b mut* compared to AB.

e) Representative image of 7 dpf immersed in cooled agarose in contact with electrodes on 12-well CytoView MEA plate.

f) Startle response behavioral assay. Light source was removed for 5 secs at 10 min intervals. Mean distance reported from tracked movement during 70 min assay. Decreased light startle response identified in *fam57b mut* compared to AB. Statistical analysis of each startle response by T-test **p ≤ 0.01, *** p ≤ 0.001, **** p ≤ 0.0001. Error bars SEM. No overall significant change in movement outside of the startle identified. AB n = 125, *fam57b mut* n = 33 over 5 experiments.

g) Seizure response behavioral assay. Normalized (baseline recording subtracted) mean distance from tracked movement after absence or presence of pentylenetetrazol (PTZ) 0.5 mM and 5 mM. Significantly increased seizure-induced movement observed at 5mM in AB, while increased movement observed at 0.5 and 5 mM PTZ in *fam57b mut*. Diminished overall seizure-induced movement at 5 mM in *fam57b mut* compared to AB. Relative fold change compared to absence of PTZ indicated below histogram. Statistical analysis of each condition by T-test *p≤ 0.05, *** p ≤ 0.001, **** p ≤ 0.0001. Error bars SEM. AB n = 166 (0 mM), 92 (0.5 mM), 150 (5 mM), *fam57b mut* n = 91 (0 mM), 70 (0.5 mM), 56 (5mM) over 6 experiments.

h) Model proposing role of Fam57b activity in the brain. Loss of function in *fam57b* mutants indicate significant changes in plasma membrane lipid groups alter architecture of plasma membrane early the developing brain. Architectural changes indicated by increased lipid raft abundance and aggregation. Altered plasma membrane homeostasis results in mis-localization of synaptic proteins, including synaptotagmins, after maturation. Decreased spontaneous brain and network activity suggests diminished synaptic function and developed circuits. As evidence has suggested spontaneous network activity shapes synaptic development, this cycles back to declined neuronal maturation and circuity. Molecular changes to synaptic function and decreased spontaneous brain activity translate to altered behavioral response after stimuli presentation.

Supplementary Tables

Table S1 - iPSC Neuron Lipidomics. Related to figure 2.

Table S2 - SH-SY5Y Lipidomics. Related to figure 4.

Table S3 - SH-SY5Y Synaptosome MSMS. Related to figure 5.

Table S4 - SH-SY5Y Synaptosome Lipidomics. Related to figure 5.

Table S5 - Zebrafish Larvae Brain Lipidomics. Related to figure 7.

Table S6 - Zebrafish Larvae Brain Biotinylation MSMS. Related to figure 7.

Table S7 - Zebrafish Larvae Brain Synaptosome MSMS. Related to figure 7.

Table S8 - Zebrafish Larvae Head and Body Measurements. Related to figure 8.

Table S9 - Zebrafish Larvae Light Startle Response Data. Related to figure 8.

Table S10 - Zebrafish Larvae Seizure Assay Data. Related to figure 8.

References

ANTONIO, C., FERBY, I., WILHELM, H., JONES, M., KARSENTI, E., NEBREDA, A. R. & VERNOS, I. 2000. Xkid, a chromokinesin required for chromosome alignment on the metaphase plate. *Cell,* 102**,** 425-35.

ARBOGAST, T., OUAGAZZAL, A. M., CHEVALIER, C., KOPANITSA, M., AFINOWI, N., MIGLIAVACCA, E., COWLING, B. S., BIRLING, M. C., CHAMPY, M. F., REYMOND, A. & HERAULT, Y. 2016. Reciprocal Effects on Neurocognitive and Metabolic Phenotypes in Mouse Models of 16p11.2 Deletion and Duplication Syndromes. *PLoS Genet,* 12**,** e1005709.

BAKER, K., GORDON, S. L., MELLAND, H., BUMBAK, F., SCOTT, D. J., JIANG, T. J., OWEN, D., TURNER, B. J., BOYD, S. G., ROSSI, M., AL-RAQAD, M., ELPELEG, O., PECK, D., MANCINI, G. M. S., WILKE, M., ZOLLINO, M., MARANGI, G., WEIGAND, H., BORGGRAEFE, I., HAACK, T., STARK, Z., SADEDIN, S., BROAD CENTER FOR MENDELIAN, G., TAN, T. Y., JIANG, Y., GIBBS, R. A., ELLINGWOOD, S., AMARAL, M., KELLEY, W., KURIAN, M. A., COUSIN, M. A. & RAYMOND, F. L. 2018. SYT1-associated neurodevelopmental disorder: a case series. *Brain,* 141**,** 2576-2591.

BARABAN, S. C., TAYLOR, M. R., CASTRO, P. A. & BAIER, H. 2005. Pentylenetetrazole induced changes in zebrafish behavior, neural activity and c-fos expression. *Neuroscience,* 131**,** 759-68.

BAYES, A., COLLINS, M. O., REIG-VIADER, R., GOU, G., GOULDING, D., IZQUIERDO, A., CHOUDHARY, J. S., EMES, R. D. & GRANT, S. G. 2017. Evolution of complexity in the zebrafish synapse proteome. *Nat Commun,* 8**,** 14613.

BAZINET, R. P. & LAYE, S. 2014. Polyunsaturated fatty acids and their metabolites in brain function and disease. *Nat Rev Neurosci,* 15**,** 771-85.

BEER, K. B., RIVAS-CASTILLO, J., KUHN, K., FAZELI, G., KARMANN, B., NANCE, J. F., STIGLOHER, C. & WEHMAN, A. M. 2018. Extracellular vesicle budding is inhibited by redundant regulators of TAT-5 flippase localization and phospholipid asymmetry. *Proc Natl Acad Sci U S A,* 115**,** E1127-E1136.

BLACKMON, K., THESEN, T., GREEN, S., BEN-AVI, E., WANG, X., FUCHS, B., KUZNIECKY, R. & DEVINSKY, O. 2018. Focal Cortical Anomalies and Language Impairment in 16p11.2 Deletion and Duplication Syndrome. *Cereb Cortex,* 28**,** 2422-2430.

BOONEN, M., STAUDT, C., GILIS, F., OORSCHOT, V., KLUMPERMAN, J. & JADOT, M. 2016. Cathepsin D and its newly identified transport receptor SEZ6L2 can modulate neurite outgrowth. *J Cell Sci,* 129**,** 557-68.

CHEN, Y., YANG, Z., MENG, M., ZHAO, Y., DONG, N., YAN, H., LIU, L., DING, M., PENG, H. B. & SHAO, F. 2009. Cullin mediates degradation of RhoA through evolutionarily conserved BTB adaptors to control actin cytoskeleton structure and cell movement. *Mol Cell,* 35**,** 841-55.

CHIOCCHETTI, A. G., HASLINGER, D., STEIN, J. L., DE LA TORRE-UBIETA, L., COCCHI, E., ROTHAMEL, T., LINDLAR, S., WALTES, R., FULDA, S., GESCHWIND, D. H. & FREITAG, C. M. 2016. Transcriptomic signatures of neuronal differentiation and their association with risk genes for autism spectrum and related neuropsychiatric disorders. *Transl Psychiatry,* 6**,** e864.

D'ANGELO, D., LEBON, S., CHEN, Q. X., MARTIN-BREVET, S., SNYDER, L. G., HIPPOLYTE, L., HANSON, E., MAILLARD, A. M., FAUCETT, W. A., MACE, A., PAIN, A., BERNIER, R.,

CHAWNER, S. J. R. A., DAVID, A., ANDRIEUX, J., AYLWARD, E., BAUJAT, G., CALDEIRA, I., CONUS, P., FERRARI, C., FORZANO, F., GERARD, M., GOIN-KOCHEL, R. P., GRANT, E., HUNTER, J. V., ISIDOR, B., JACQUETTE, A., JONCH, A. E., KEREN, B., LACOMBE, D., LE CAIGNEC, C., MARTIN, C. L., MAANNIK, K., METSPALU, A., MIGNOT, C., MUKHERJEE, P., OWEN, M. J., PASSEGGERI, M., ROORYCK-THAMBO, C., ROSENFELD, J. A., SPENCE, S. J., STEINMAN, K. J., TJERNAGEL, J., VAN HAELST, M., SHEN, Y. P., DRAGANSKI, B., SHERR, E. H., LEDBETTER, D. H., VAN DEN BREE, M. B. M., BECKMANN, J. S., SPIRO, J. E., REYMOND, A., JACQUEMONT, S., CHUNG, W. K., CHILDREN, C. U. E., CONSORTIUM, P. E. & PROJE, S. V. I. 2016. Defining the Effect of the 16p11.2 Duplication on Cognition, Behavior, and Medical Comorbidities. *Jama Psychiatry,* 73**,** 20-30.

DE ANDA, F. C., ROSARIO, A. L., DURAK, O., TRAN, T., GRAFF, J., MELETIS, K., REI, D., SODA, T., MADABHUSHI, R., GINTY, D. D., KOLODKIN, A. L. & TSAI, L. H. 2012. Autism spectrum disorder susceptibility gene TAOK2 affects basal dendrite formation in the neocortex. *Nat Neurosci,* 15**,** 1022-31.

DESHPANDE, A., YADAV, S., DAO, D. Q., WU, Z. Y., HOKANSON, K. C., CAHILL, M. K., WIITA, A. P., JAN, Y. N., ULLIAN, E. M. & WEISS, L. A. 2017. Cellular Phenotypes in Human iPSC-Derived Neurons from a Genetic Model of Autism Spectrum Disorder. *Cell Rep,* 21**,** 2678-2687.

DZIOBEK, I., GOLD, S. M., WOLF, O. T. & CONVIT, A. 2007. Hypercholesterolemia in Asperger syndrome: independence from lifestyle, obsessive-compulsive behavior, and social anxiety. *Psychiatry Res,* 149**,** 321-4.

EGAWA, J., WATANABE, Y., WANG, C., INOUE, E., SUGIMOTO, A., SUGIYAMA, T., IGETA, H., NUNOKAWA, A., SHIBUYA, M., KUSHIMA, I., ORIME, N., HAYASHI, T., OKADA, T., UNO, Y., OZAKI, N. & SOMEYA, T. 2015. Novel rare missense variations and risk of autism spectrum disorder: whole-exome sequencing in two families with affected siblings and a two-stage follow-up study in a Japanese population. *PLoS One,* 10**,** e0119413.

EGOLF, L. E., VAKSMAN, Z., LOPEZ, G., ROKITA, J. L., MODI, A., BASTA, P. V., HAKONARSON, H., OLSHAN, A. F. & DISKIN, S. J. 2019. Germline 16p11.2 Microdeletion Predisposes to Neuroblastoma. *Am J Hum Genet,* 105**,** 658-668.

FERNANDEZ, I., ARAC, D., UBACH, J., GERBER, S. H., SHIN, O., GAO, Y., ANDERSON, R. G., SUDHOF, T. C. & RIZO, J. 2001. Three-dimensional structure of the synaptotagmin 1 C2B-domain: synaptotagmin 1 as a phospholipid binding machine. *Neuron,* 32**,** 1057-69.

FETIT, R., PRICE, D. J., LAWRIE, S. M. & JOHNSTONE, M. 2020. Understanding the clinical manifestations of 16p11.2 deletion syndrome: a series of developmental case reports in children. *Psychiatr Genet,* 30**,** 136-140.

FISHMAN, P. H., MOSS, J. & OSBORNE, J. C., JR. 1978. Interaction of choleragen with the oligosaccharide of ganglioside GM1: evidence for multiple oligosaccharide binding sites. *Biochemistry,* 17**,** 711-6.

FLIS, V. V. & DAUM, G. 2013. Lipid transport between the endoplasmic reticulum and mitochondria. *Cold Spring Harb Perspect Biol,* 5.

GIANNUZZI, G., SCHMIDT, P. J., PORCU, E., WILLEMIN, G., MUNSON, K. M., NUTTLE, X., EARL, R., CHRAST, J., HOEKZEMA, K., RISSO, D., MANNIK, K., DE NITTIS, P., BARATZ, E. D., P, C., HERAULT, Y., GAO, X., PHILPOTT, C. C., BERNIER, R. A., KUTALIK, Z., FLEMING, M. D., EICHLER, E. E. & REYMOND, A. 2019. The Human-Specific BOLA2 Duplication Modifies Iron Homeostasis and Anemia Predisposition in Chromosome 16p11.2 Autism Individuals. *Am J Hum Genet,* 105**,** 947-958.

GIOVANNIELLO, J. A., S.; YU, K.; LI, B. 2021. Sex-Specific Stress-Related Behavioral Phenotypes and Central Amygdala Dysfunction in a Mouse Model of 16p11.2 Microdeletion. *Biological Psychiatry Global Open Science,* 1**,** 59 - 69.

GOLZIO, C., WILLER, J., TALKOWSKI, M. E., OH, E. C., TANIGUCHI, Y., JACQUEMONT, S., REYMOND, A., SUN, M., SAWA, A., GUSELLA, J. F., KAMIYA, A., BECKMANN, J. S. & KATSANIS, N. 2012. KCTD13 is a major driver of mirrored neuroanatomical phenotypes of the 16p11.2 copy number variant. *Nature,* 485**,** 363-7.

GROSCH, S., SCHIFFMANN, S. & GEISSLINGER, G. 2012. Chain length-specific properties of ceramides. *Prog Lipid Res,* 51**,** 50-62.

GUSTAVSSON, N. & HAN, W. 2009. Calcium-sensing beyond neurotransmitters: functions of synaptotagmins in neuroendocrine and endocrine secretion. *Biosci Rep,* 29**,** 245-59.

HANSON, E., BERNIER, R., PORCHE, K., JACKSON, F. I., GOIN-KOCHEL, R. P., SNYDER, L. G., SNOW, A. V., WALLACE, A. S., CAMPE, K. L., ZHANG, Y., CHEN, Q. X., D'ANGELO, D., MORENO-DE-LUCA, A., ORR, P. T., BOOMER, K. B., EVANS, D. W., KANNE, S., BERRY, L., MILLER, F. K., OLSON, J., SHERR, E., MARTIN, C. L., LEDBETTER, D. H., SPIRO, J. E., CHUNG, W. K. & PROJE, S. V. I. 2015. The Cognitive and Behavioral Phenotype of the 16p11.2 Deletion in a Clinically Ascertained Population. *Biological Psychiatry,* 77**,** 785-793.

HASLINGER, D., WALTES, R., YOUSAF, A., LINDLAR, S., SCHNEIDER, I., LIM, C. K., TSAI, M. M., GARVALOV, B. K., ACKER-PALMER, A., KREZDORN, N., ROTTER, B., ACKER, T., GUILLEMIN, G. J., FULDA, S., FREITAG, C. M. & CHIOCCHETTI, A. G. 2018. Loss of the Chr16p11.2 ASD candidate gene QPRT leads to aberrant neuronal differentiation in the SH-SY5Y neuronal cell model. *Mol Autism,* 9**,** 56.

HINKLEY, L. B. N., DALE, C. L., LUKS, T. L., FINDLAY, A. M., BUKSHPUN, P., POJMAN, N., THIEU, T., CHUNG, W. K., BERMAN, J., ROBERTS, T. P. L., MUKHERJEE, P., SHERR, E. H. & NAGARAJAN, S. S. 2019. Sensorimotor Cortical Oscillations during Movement Preparation in 16p11.2 Deletion Carriers. *J Neurosci,* 39**,** 7321-7331.

HOYTEMA VAN KONIJNENBURG, E. M. M., LUIRINK, I. K., SCHAGEN, S. E. E., ENGELEN, M., BERENDSE, K., POLL-THE, B. T. & CHEGARY, M. 2020. Hyperinsulinism in a patient with a Zellweger Spectrum Disorder and a 16p11.2 deletion syndrome. *Mol Genet Metab Rep,* 23**,** 100590.

IP, J. P. K., NAGAKURA, I., PETRAVICZ, J., LI, K., WIEMER, E. A. C. & SUR, M. 2018. Major Vault Protein, a Candidate Gene in 16p11.2 Microdeletion Syndrome, Is Required for the Homeostatic Regulation of Visual Cortical Plasticity. *J Neurosci,* 38**,** 3890-3900.

KALUEFF, A. V., STEWART, A. M. & GERLAI, R. 2014. Zebrafish as an emerging model for studying complex brain disorders. *Trends Pharmacol Sci,* 35**,** 63-75.

KIKUMA, K., LI, X., KIM, D., SUTTER, D. & DICKMAN, D. K. 2017. Extended Synaptotagmin Localizes to Presynaptic ER and Promotes Neurotransmission and Synaptic Growth in Drosophila. *Genetics,* 207**,** 993-1006.

KIM, S. H., GREEN-SNYDER, L., LORD, C., BISHOP, S., STEINMAN, K. J., BERNIER, R., HANSON, E., GOIN-KOCHEL, R. P. & CHUNG, W. K. 2020. Language characterization in 16p11.2 deletion and duplication syndromes. *Am J Med Genet B Neuropsychiatr Genet,* 183**,** 380-391.

KLEINENDORST, L., VAN DEN HEUVEL, L. M., HENNEMAN, L. & VAN HAELST, M. M. 2020. Who ever heard of 16p11.2 deletion syndrome? Parents' perspectives on a susceptibility copy number variation syndrome. *Eur J Hum Genet,* 28**,** 1196-1204.

KOVALEVICH J, L. D. 2013. Considerations for the Use of SH-SY5Y Neuroblastoma Cells in Neurobiology. *Methods Mol Biol***,** 9-21.

KRAFT, M. L. 2016. Sphingolipid Organization in the Plasma Membrane and the Mechanisms That Influence It. *Front Cell Dev Biol,* 4**,** 154.

LAI, A. L., TAMM, L. K., ELLENA, J. F. & CAFISO, D. S. 2011. Synaptotagmin 1 modulates lipid acyl chain order in lipid bilayers by demixing phosphatidylserine. *J Biol Chem,* 286**,** 25291-300.

LEVY, M. & FUTERMAN, A. H. 2010. Mammalian ceramide synthases. *IUBMB Life,* 62**,** 347-56.

LI, Y. C., CHANADAY, N. L., XU, W. & KAVALALI, E. T. 2017. Synaptotagmin-1- and Synaptotagmin-7-Dependent Fusion Mechanisms Target Synaptic Vesicles to Kinetically Distinct Endocytic Pathways. *Neuron,* 93**,** 616-631 e3.

LIN, G. N., COROMINAS, R., LEMMENS, I., YANG, X., TAVERNIER, J., HILL, D. E., VIDAL, M., SEBAT, J. & IAKOUCHEVA, L. M. 2015. Spatiotemporal 16p11.2 protein network implicates cortical late mid-fetal brain development and KCTD13-Cul3-RhoA pathway in psychiatric diseases. *Neuron,* 85**,** 742-54.

LOHNER, K. 1996. Is the high propensity of ethanolamine plasmalogens to form non-lamellar lipid structures manifested in the properties of biomembranes? *Chem Phys Lipids,* 81**,** 167-84.

MAILLARD, A. M., RUEF, A., PIZZAGALLI, F., MIGLIAVACCA, E., HIPPOLYTE, L., ADASZEWSKI, S., DUKART, J., FERRARI, C., CONUS, P., MANNIK, K., ZAZHYTSKA, M., SIFFREDI, V., MAEDER, P., KUTALIK, Z., KHERIF, F., HADJIKHANI, N., BECKMANN, J. S., REYMOND, A., DRAGANSKI, B., JACQUEMONT, S. & P11.2 EUROPEAN, C. 2015. The 16p11.2 locus modulates brain structures common to autism, schizophrenia and obesity. *Mol Psychiatry,* 20**,** 140-7.

MARCONESCU, A. & THORPE, P. E. 2008. Coincident exposure of phosphatidylethanolamine and anionic phospholipids on the surface of irradiated cells. *Biochim Biophys Acta,* 1778**,** 2217-24.

MARTIN LORENZO, S., NALESSO, V., CHEVALIER, C., BIRLING, M. C. & HERAULT, Y. 2021. Targeting the RHOA pathway improves learning and memory in adult Kctd13 and 16p11.2 deletion mouse models. *Mol Autism,* 12**,** 1.

MARTIN-BREVET, S., RODRIGUEZ-HERREROS, B., NIELSEN, J. A., MOREAU, C., MODENATO, C., MAILLARD, A. M., PAIN, A., RICHETIN, S., JONCH, A. E., QURESHI, A. Y., ZURCHER, N. R., CONUS, P., P11.2 EUROPEAN, C., SIMONS VARIATION IN INDIVIDUALS PROJECT, C., CHUNG, W. K., SHERR, E. H., SPIRO, J. E., KHERIF, F., BECKMANN, J. S., HADJIKHANI, N., REYMOND, A., BUCKNER, R. L., DRAGANSKI, B. & JACQUEMONT, S. 2018. Quantifying the Effects of 16p11.2 Copy Number Variants on Brain Structure: A Multisite Genetic-First Study. *Biol Psychiatry,* 84**,** 253-264.

MCCAMMON, J. M., BLAKER-LEE, A., CHEN, X. & SIVE, H. 2017. The 16p11.2 homologs fam57ba and doc2a generate certain brain and body phenotypes. *Hum Mol Genet,* 26**,** 3699-3712.

MCCAMMON, J. M. & SIVE, H. 2015. Challenges in understanding psychiatric disorders and developing therapeutics: a role for zebrafish. *Dis Model Mech,* 8**,** 647-56.

MEFFORD, H. C., YENDLE, S. C., HSU, C., COOK, J., GERAGHTY, E., MCMAHON, J. M., EEG-OLOFSSON, O., SADLEIR, L. G., GILL, D., BEN-ZEEV, B., LERMAN-SAGIE, T., MACKAY, M., FREEMAN, J. L., ANDERMANN, E., PELAKANOS, J. T., ANDREWS, I., WALLACE, G., EICHLER, E. E., BERKOVIC, S. F. & SCHEFFER, I. E. 2011. Rare copy number variants are an important cause of epileptic encephalopathies. *Ann Neurol,* 70**,** 974-85.

NIARCHOU, M., CHAWNER, S., DOHERTY, J. L., MAILLARD, A. M., JACQUEMONT, S., CHUNG, W. K., GREEN-SNYDER, L., BERNIER, R. A., GOIN-KOCHEL, R. P., HANSON, E., LINDEN, D. E. J., LINDEN, S. C., RAYMOND, F. L., SKUSE, D., HALL, J., OWEN, M. J. & VAN DEN BREE, M. B. M. 2019. Correction: Psychiatric disorders in children with 16p11.2 deletion and duplication. *Transl Psychiatry,* 9**,** 107.

OHSUGI, M., ADACHI, K., HORAI, R., KAKUTA, S., SUDO, K., KOTAKI, H., TOKAI-NISHIZUMI, N., SAGARA, H., IWAKURA, Y. & YAMAMOTO, T. 2008. Kid-mediated chromosome compaction ensures proper nuclear envelope formation. *Cell,* 132**,** 771-82.

OUELLETTE, J., TOUSSAY, X., COMIN, C. H., COSTA, L. D. F., HO, M., LACALLE-AURIOLES, M., FREITAS-ANDRADE, M., LIU, Q. Y., LECLERC, S., PAN, Y., LIU, Z., THIBODEAU, J. F., YIN, M., CARRIER, M., MORSE, C. J., DYKEN, P. V., BERGIN, C. J., BAILLET, S., KENNEDY, C. R., TREMBLAY, M. E., BENOIT, Y. D., STANFORD, W. L., BURGER, D., STEWART, D. J. & LACOSTE, B. 2020. Vascular contributions to 16p11.2 deletion autism syndrome modeled in mice. *Nat Neurosci,* 23**,** 1090-1101.

OWEN, J. P., BUKSHPUN, P., POJMAN, N., THIEU, T., CHEN, Q., LEE, J., D'ANGELO, D., GLENN, O. A., HUNTER, J. V., BERMAN, J. I., ROBERTS, T. P., BUCKNER, R., NAGARAJAN, S. S., MUKHERJEE, P. & SHERR, E. H. 2018. Brain MR Imaging Findings and Associated Outcomes in Carriers of the Reciprocal Copy Number Variation at 16p11.2. *Radiology,* 286**,** 217-226.

PALTAUF, F. 1994. Ether lipids in biomembranes. *Chem Phys Lipids,* 74**,** 101-39.

PARK, S. M., LITTLETON, J. T., PARK, H. R. & LEE, J. H. 2016. Drosophila Homolog of Human KIF22 at the Autism-Linked 16p11.2 Loci Influences Synaptic Connectivity at Larval Neuromuscular Junctions. *Exp Neurobiol,* 25**,** 33-9.

PEWZNER-JUNG, Y., BEN-DOR, S. & FUTERMAN, A. H. 2006. When do Lasses (longevity assurance genes) become CerS (ceramide synthases)?: Insights into the regulation of ceramide synthesis. *J Biol Chem,* 281**,** 25001-5.

PIKE, L. J. 2003. Lipid rafts: bringing order to chaos. *J Lipid Res,* 44**,** 655-67.

PINTO, D., PAGNAMENTA, A. T., KLEI, L., ANNEY, R., MERICO, D., REGAN, R., CONROY, J., MAGALHAES, T. R., CORREIA, C., ABRAHAMS, B. S., ALMEIDA, J., BACCHELLI, E., BADER, G. D., BAILEY, A. J., BAIRD, G., BATTAGLIA, A., BERNEY, T., BOLSHAKOVA, N., BOLTE, S., BOLTON, P. F., BOURGERON, T., BRENNAN, S., BRIAN, J., BRYSON, S. E., CARSON, A. R., CASALLO, G., CASEY, J., CHUNG, B. H., COCHRANE, L., CORSELLO, C., CRAWFORD, E. L., CROSSETT, A., CYTRYNBAUM, C., DAWSON, G., DE JONGE, M., DELORME, R., DRMIC, I., DUKETIS, E., DUQUE, F., ESTES, A., FARRAR, P., FERNANDEZ, B. A., FOLSTEIN, S. E., FOMBONNE, E., FREITAG, C. M., GILBERT, J., GILLBERG, C., GLESSNER, J. T., GOLDBERG, J., GREEN, A., GREEN, J., GUTER, S. J., HAKONARSON, H., HERON, E. A., HILL, M., HOLT, R., HOWE, J. L., HUGHES, G., HUS, V., IGLIOZZI, R., KIM, C., KLAUCK, S. M., KOLEVZON, A., KORVATSKA, O., KUSTANOVICH, V., LAJONCHERE, C. M., LAMB, J. A., LASKAWIEC, M., LEBOYER, M., LE COUTEUR, A., LEVENTHAL, B. L., LIONEL, A. C., LIU, X. Q., LORD, C., LOTSPEICH, L., LUND, S. C., MAESTRINI, E., MAHONEY, W., MANTOULAN, C., MARSHALL, C. R., MCCONACHIE, H., MCDOUGLE, C. J., MCGRATH, J., MCMAHON, W. M., MERIKANGAS, A., MIGITA, O., MINSHEW, N. J., MIRZA, G. K., MUNSON, J., NELSON, S. F., NOAKES, C., NOOR, A., NYGREN, G., OLIVEIRA, G., PAPANIKOLAOU, K., PARR, J. R., PARRINI, B., PATON, T., PICKLES, A., PILORGE, M., et al. 2010. Functional impact of global rare copy number variation in autism spectrum disorders. *Nature,* 466**,** 368-72.

QURESHI, A. Y., MUELLER, S., SNYDER, A. Z., MUKHERJEE, P., BERMAN, J. I., ROBERTS, T. P., NAGARAJAN, S. S., SPIRO, J. E., CHUNG, W. K., SHERR, E. H., BUCKNER, R. L. & SIMONS, V. I. P. C. 2014. Opposing brain differences in 16p11.2 deletion and duplication carriers. *J Neurosci,* 34**,** 11199-211.

RANTA, S., ZHANG, Y., ROSS, B., LONKA, L., TAKKUNEN, E., MESSER, A., SHARP, J., WHEELER, R., KUSUMI, K., MOLE, S., LIU, W., SOARES, M. B., BONALDO, M. F., HIRVASNIEMI, A., DE LA CHAPELLE, A., GILLIAM, T. C. & LEHESJOKI, A. E. 1999. The neuronal ceroid lipofuscinoses in human EPMR and mnd mutant mice are associated with mutations in CLN8. *Nat Genet,* 23**,** 233-6.

SATTERSTROM, F. K., WALTERS, R. K., SINGH, T., WIGDOR, E. M., LESCAI, F., DEMONTIS, D., KOSMICKI, J. A., GROVE, J., STEVENS, C., BYBJERG-GRAUHOLM, J., BAEKVAD-HANSEN, M., PALMER, D. S., MALLER, J. B., I, P.-B. C., NORDENTOFT, M., MORS, O., ROBINSON, E. B., HOUGAARD, D. M., WERGE, T. M., BO MORTENSEN, P., NEALE, B. M., BORGLUM, A. D. & DALY, M. J. 2019. Autism spectrum disorder and attention deficit hyperactivity disorder have a similar burden of rare protein-truncating variants. *Nat Neurosci,* 22**,** 1961-1965.

SCHONN, J. S., MAXIMOV, A., LAO, Y., SUDHOF, T. C. & SORENSEN, J. B. 2008. Synaptotagmin-1 and -7 are functionally overlapping Ca2+ sensors for exocytosis in adrenal chromaffin cells. *Proc Natl Acad Sci U S A,* 105**,** 3998-4003.

SEBAT, J., LAKSHMI, B., MALHOTRA, D., TROGE, J., LESE-MARTIN, C., WALSH, T., YAMROM, B., YOON, S., KRASNITZ, A., KENDALL, J., LEOTTA, A., PAI, D., ZHANG, R., LEE, Y. H., HICKS, J., SPENCE, S. J., LEE, A. T., PUURA, K., LEHTIMAKI, T., LEDBETTER, D., GREGERSEN, P. K., BREGMAN, J., SUTCLIFFE, J. S., JOBANPUTRA, V., CHUNG, W., WARBURTON, D., KING, M. C., SKUSE, D., GESCHWIND, D. H., GILLIAM, T. C., YE, K. & WIGLER, M. 2007. Strong association of de novo copy number mutations with autism. *Science,* 316**,** 445-9.

SIMONS VIP, C. 2012. Simons Variation in Individuals Project (Simons VIP): a genetics-first approach to studying autism spectrum and related neurodevelopmental disorders. *Neuron,* 73**,** 1063-7.

SORENSEN, J. B., FERNANDEZ-CHACON, R., SUDHOF, T. C. & NEHER, E. 2003. Examining synaptotagmin 1 function in dense core vesicle exocytosis under direct control of Ca2+. *J Gen Physiol,* 122**,** 265-76.

STEWART, A. M., NGUYEN, M., WONG, K., POUDEL, M. K. & KALUEFF, A. V. 2014. Developing zebrafish models of autism spectrum disorder (ASD). *Prog Neuropsychopharmacol Biol Psychiatry,* 50**,** 27-36.

TIDHAR, R., BEN-DOR, S., WANG, E., KELLY, S., MERRILL, A. H., JR. & FUTERMAN, A. H. 2012. Acyl chain specificity of ceramide synthases is determined within a region of 150 residues in the Tram-Lag-CLN8 (TLC) domain. *J Biol Chem,* 287**,** 3197-206.

TIERNEY, E., BUKELIS, I., THOMPSON, R. E., AHMED, K., ANEJA, A., KRATZ, L. & KELLEY, R. I. 2006. Abnormalities of cholesterol metabolism in autism spectrum disorders. *Am J Med Genet B Neuropsychiatr Genet,* 141B**,** 666-8.

TOMASELLO, D. L. & SIVE, H. 2020. Noninvasive Multielectrode Array for Brain and Spinal Cord Local Field Potential Recordings from Live Zebrafish Larvae. *Zebrafish,* 17**,** 271-277.

TRACEY, T. J., STEYN, F. J., WOLVETANG, E. J. & NGO, S. T. 2018. Neuronal Lipid Metabolism: Multiple Pathways Driving Functional Outcomes in Health and Disease. *Front Mol Neurosci,* 11**,** 10.

VANNI, N., FRUSCIONE, F., FERLAZZO, E., STRIANO, P., ROBBIANO, A., TRAVERSO, M., SANDER, T., FALACE, A., GAZZERRO, E., BRAMANTI, P., BIELAWSKI, J., FASSIO, A., MINETTI, C., GENTON, P. & ZARA, F. 2014. Impairment of ceramide synthesis causes a novel progressive myoclonus epilepsy. *Ann Neurol,* 76**,** 206-12.

WORSTELL, N. C., KRISHNAN, P., WEATHERSTON, J. D. & WU, H. J. 2016. Binding Cooperativity Matters: A GM1-Like Ganglioside-Cholera Toxin B Subunit Binding Study Using a Nanocube-Based Lipid Bilayer Array. *PLoS One,* 11**,** e0153265.

XI, Y., NOBLE, S. & EKKER, M. 2011. Modeling neurodegeneration in zebrafish. *Curr Neurol Neurosci Rep,* 11**,** 274-82.

XU, J., MASHIMO, T. & SUDHOF, T. C. 2007. Synaptotagmin-1, -2, and -9: Ca(2+) sensors for fast release that specify distinct presynaptic properties in subsets of neurons. *Neuron,* 54**,** 567-81.

YAMASHITA-SUGAHARA, Y., TOKUZAWA, Y., NAKACHI, Y., KANESAKI-YATSUKA, Y., MATSUMOTO, M., MIZUNO, Y. & OKAZAKI, Y. 2013. Fam57b (family with sequence similarity 57, member B), a novel peroxisome proliferator-activated receptor gamma target gene that regulates adipogenesis through ceramide synthesis. *J Biol Chem,* 288**,** 4522-37.

YU, H., LIU, Y., GULBRANSON, D. R., PAINE, A., RATHORE, S. S. & SHEN, J. 2016. Extended synaptotagmins are Ca2+-dependent lipid transfer proteins at membrane contact sites. *Proc Natl Acad Sci U S A,* 113**,** 4362-7.

YUAN, A. & NIXON, R. A. 2016. Specialized roles of neurofilament proteins in synapses: Relevance to neuropsychiatric disorders. *Brain Res Bull,* 126**,** 334-346.

ZHANG, T., TRAUGER, S. A., VIDOUDEZ, C., DOANE, K. P., PLUIMER, B. R. & PETERSON, R. T. 2019. Parallel Reaction Monitoring reveals structure-specific ceramide alterations in the zebrafish. *Sci Rep,* 9**,** 19939.

ZUFFEREY, F., SHERR, E. H., BECKMANN, N. D., HANSON, E., MAILLARD, A. M., HIPPOLYTE, L., MACE, A., FERRARI, C., KUTALIK, Z., ANDRIEUX, J., AYLWARD, E., BARKER, M., BERNIER, R., BOUQUILLON, S., CONUS, P., DELOBEL, B., FAUCETT, W., GOIN-KOCHEL, R. P., GRANT, E., HAREWOOD, L., HUNTER, J. V., LEBON, S., LEDBETTER, D. H., MARTIN, C. L., MANNIK, K., MARTINET, D., MUKHERJEE, P., RAMOCKI, M. B., SPENCE, S. J., STEINMAN, K. J., TJERNAGEL, J., SPIRO, J. E., REYMOND, A., BECKMANN, J. S., CHUNG, W. K., JACQUEMONT, S., CONSORTIUM, S. V. & CONSORTIUM, P.-E. 2012. A 600 kb deletion syndrome at 16p11.2 leads to energy imbalance and neuropsychiatric disorders. *Journal of Medical Genetics,* 49**,** 660-668.

REAGENT or RESOURCE	SOURCE	IDENTIFIER
Antibodies		
Synaptotagmin-1	Lifespan Bioscience	LS-B12889
GAD65 + 67	Abcam	ab11070
Beta-Actin	Proteintech	60008-1
DAPI	Life Technologies	D1306
555-Phalloidin	Invitrogen	A34055
488 anti-goat	Jackson	805-545-180,
488 anti-mouse	Jackson	715-545-151
594 anti-mouse	Jackson	715-585-150
594 anti-rabbit	Jackson	711-585-152
anti-mouse 680	Jackson	715-625-150
anti-rabbit 680	Jackson	711-625-152
VGlut1/2	Synaptic Systems	135503
PSD95	Abcam	ab18258
Ac-Tubulin	Abcam	ab179513
Prolong Gold Antifade with DAPI	LifeTech	P36935
HA	Abcam	ab18181
FLAG	Abcam	ab1162
GAPDH	Abcam	ab8245
Li-Cor 800CW Rabbit	Li-Cor	92632211
Li-Cor 680RD Mouse	Li-Cor	92668070
Chemicals, peptides, and recombinant proteins		
Matrigel	Corning	CB-40234A
mTeSR+	STEMCELL Tech	85850
Y27632	STEMCELL Tech	72302
ReLeSR	STEMCELL Tech	05872
Accutase	STEMCELL Tech	07922
DMEM/F12/HEPES	Thermo	12400024
Neurobasal	Thermo	21103049
N2	Gibco	17502048
Gem21	GeminiBio	400-160
MEM NEAA	Thermo	11140050
GlutaMAX	Gibco	35050061
Gem21 - Vit A	GeminiBio	400161
Beta-Mercaptoethanol	Sigma	M3148
FGF	Peprotech	100-18B
BDNF	Peprotech	450-02
GDNF	Peprotech	450-10
Dorsomorphin	Tocis	3093
Poly-D-Lysine	Thermo	A3890401
Laminin	Sigma	L2020
EMEM	ATCC	30-2003
F12	ATCC	30-2006
FBS	Sigma	12306C
All-trans-RA	Sigma	R2625
DMEM	Corning	MT15017CV
Polyethylenimine	Sigma	08719

Protease Inhibitor Cocktail	Sigma	200-664-3
NBD-spinganine	Avanti Polar	810206P
BSA -FA	Sigma	10775835001
16.1 Coenzyme A	Avanti Polar	870743
24.1 Coenzyme 1	Avanti Polar	870725
CT-B	Invitrogen	C34775
Duramycin-Cy3	Molecular Targeting	D-1006
SHIELD	LifeCanvas Tech	https://lifecanvastech.com/products/shield
PFA	EMS	50-970-495
RIPA	Thermo	89900
SYN-Per	Thermo	87793
Critical commercial assays		
Pierce Cell Surface Protein Isolation Kit	Thermo	89881
Deposited data		
Lipidomics	This Paper	Supplemental Excel
Biotinylation Proteomics	This Paper	Supplemental Excel
Synaptosome Proteomics	This Paper	Supplemental Excel
Experimental models: Cell lines		
SH-SY5Y	ATCC	CRL-2266
HEK293T	ATCC	CRL-3216
IPSC 16pdel 1453	Simons VIP	SV0001453
IPSC 16pdel 1455	Simons VIP	SV0001455
IPSC 16pdel 1459	Simons VIP	SV0001459
IPSC 16pdel 1473	Simons VIP	SV0001473
IPSC 16pdel 1481	Simons VIP	SV0001481
IPSC 16pdel 1495	Simons VIP	SV0001495
IPSC 16pdel 3104	Simons VIP	SS0013104
IPSC CTR 599	Corriell Institute Biobank	AG07599
IPSC CTR 675	Corriell Institute Biobank	AG07657
Experimental models: Organisms/strains		
fam57ba$^{-/-}$;*fam57bb*$^{-/-}$ Zebrafish	This Paper	
FAM57B HET SH-SY5Y	This Paper	
FAM57B KO SH-SY5Y	This Paper	
FAM57B AAVS1 SH-SY5Y	This Paper	
Oligonucleotides		
fam57bb 5’ to 3’ TAGGTGATGTCCTGGCAGGAAG	This Paper	
fam57bb 3’ to 5’ AAACCTTCCTGCCAGGACATCA	This Paper	
sgFAM57B1 5’ to 3’ - GGTGCTCCACCATGCCGCCA	This Paper	
sgFAM57B2 5’ to 3’ - GGGCACAGCAAATTGCGTGT	This Paper	
sgAAVS1 5’ to 3’ - CACCGGGGCCACTAGGGACAGGAT	This Paper	
Recombinant DNA		
FAM57B-Flag	This Paper	
CerS2-HA	This Paper	

CerS5-HA	This Paper	
CerS6-HA	This Paper	
Software and algorithms		
AxIS and Neural Metric Tool	Axion Biosystems	Axionbiosystems.com
FIJI ImageJ	ImageJ	Imagej.net
GO SLIM analysis	PANTHER	pantherdb.org
LipidSearch	Thermo Scientific	IQLAAEGABSFAPCMBFK
Mascot	Matrix Science	Matrixscience.com
Scaffold Q+S	Proteome Software	Proteomesoftware.com
PEAKS Studio 8.5	Bioinformatics Solutions Inc.	Bioinfor.com
EthoVision XT	Noldus	Noldus.com

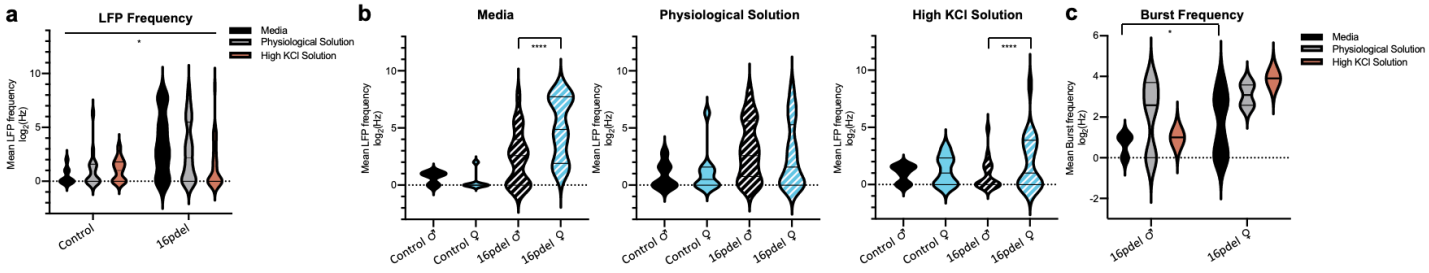

Figure 1. Augmented local field potential activity in 16pdel syndrome differentiated neuronal culture.

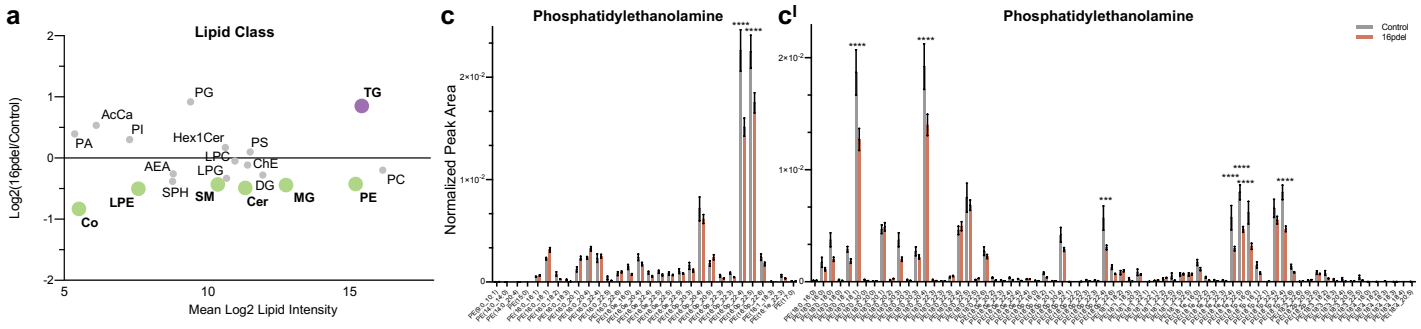

b

Composition	Saturation				Chain Length							
	Control		16pdel		Control				16pdel			
	Unsaturated	Saturated	Unsaturated	Saturated	Short	Long	Very Long	Unresolved	Short	Long	Very Long	Unresolved
AcCa	33.78%	66.22%	55.16%	44.84%		100.00%				100.00%		
AEA	100.00%		100.00%			100.00%				100.00%		
Cer	50.91%	49.09%	58.11%	41.89%		71.33%	24.35%	4.32%		70.27%	27.02%	2.71%
ChE	100.00%		100.00%			40.85%	59.15%			37.77%	62.23%	
Co					100.00%				100.00%			
DG	43.07%	56.93%	46.39%	53.61%		92.79%	7.21%			90.41%	9.59%	
Hex1Cer	54.25%	45.75%	55.70%	44.30%		49.68%	34.86%	15.47%		48.90%	36.09%	15.01%
LPC	26.32%	73.68%	33.20%	66.80%		85.26%	8.76%	5.98%		88.98%	7.84%	3.19%
LPE	74.78%	25.22%	72.99%	27.01%		73.22%	26.78%			73.09%	26.91%	
LPG	100.00%		100.00%			85.67%	14.33%			75.77%	24.23%	
MG	8.20%	91.80%	10.00%	90.00%		100.00%				100.00%		
PA	100.00%		100.00%				50.00%	50.00%			50.00%	50.00%
PC	46.37%	53.63%	55.94%	44.06%		15.94%	42.95%	41.11%		17.85%	42.35%	39.80%
PE	60.77%	39.23%	60.31%	39.69%		71.18%	27.33%	1.48%		71.82%	26.75%	1.43%
PG	90.12%	9.88%	94.38%	5.62%	1.34%	71.78%	26.77%	0.11%	0.48%	51.88%	47.59%	0.05%
PI	77.67%	22.33%	77.31%	22.69%		82.40%	13.17%	4.43%		81.22%	16.43%	2.35%
PS	100.00%		100.00%			60.01%	39.94%	0.05%		58.49%	41.19%	0.31%
SM	98.40%	1.60%	99.26%	0.74%		0.62%	50.01%	49.37%		0.74%	50.03%	49.22%
SPH	51.33%	48.67%	50.79%	49.21%		100.00%				100.00%		
TG	71.15%	28.85%	80.28%	19.72%	0.01%	94.53%	5.03%	0.43%		90.12%	9.67%	0.20%

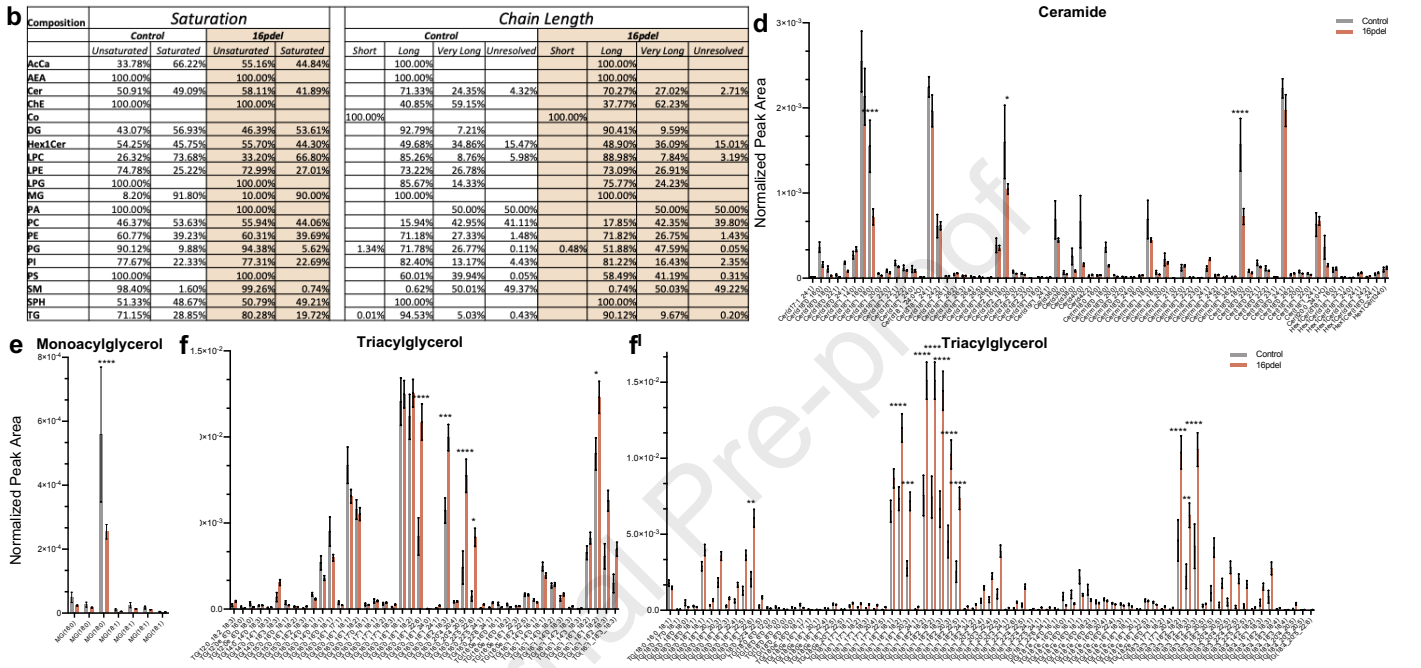

Figure 2. Significant lipid changes between control and 16pdel differentiated neurons.

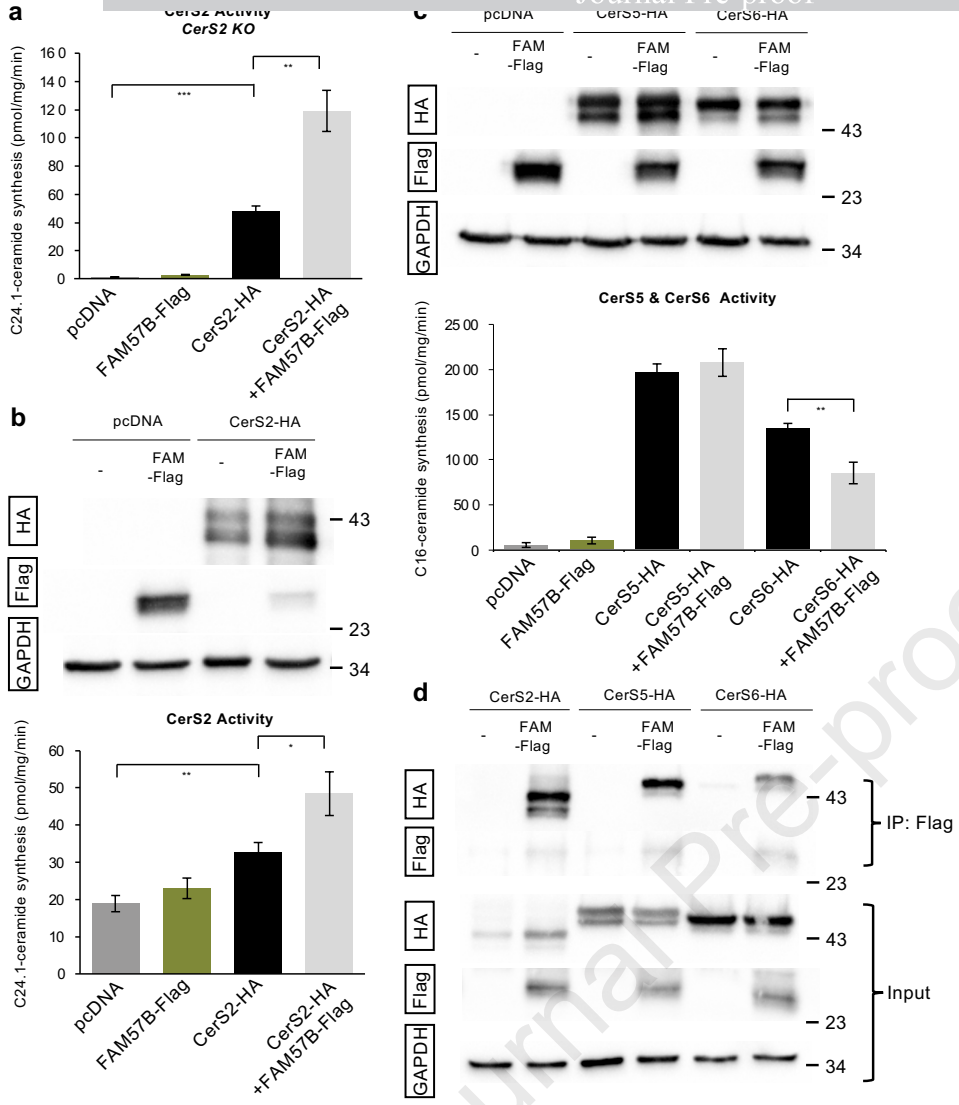

Figure 3. FAM57B interacts with CerS but does not have CerS activity.

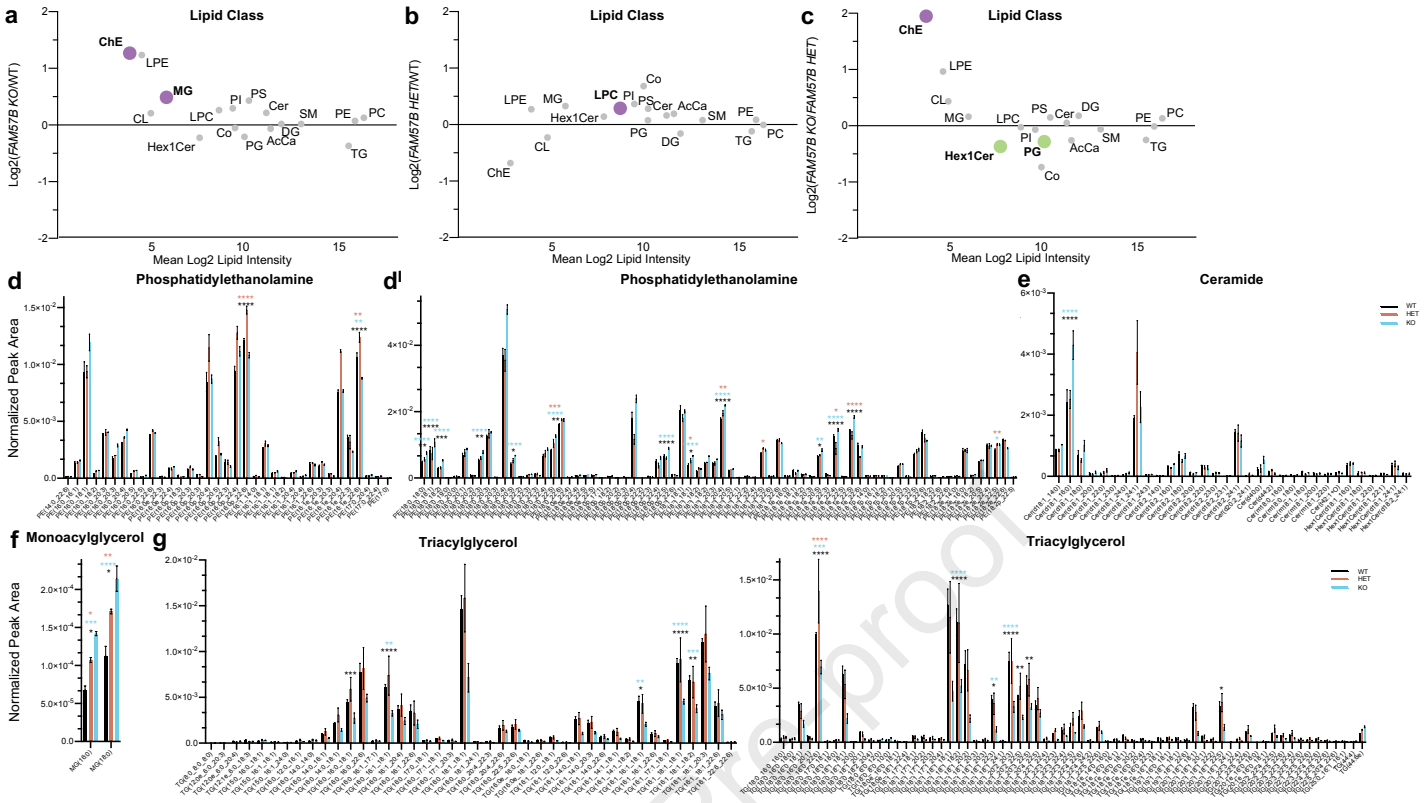

Figure 4. Significant lipid changes in sphingolipids and glycerolipids between WT and *FAM57B mutant* human differentiated SH-SY5Y neuronal cells.

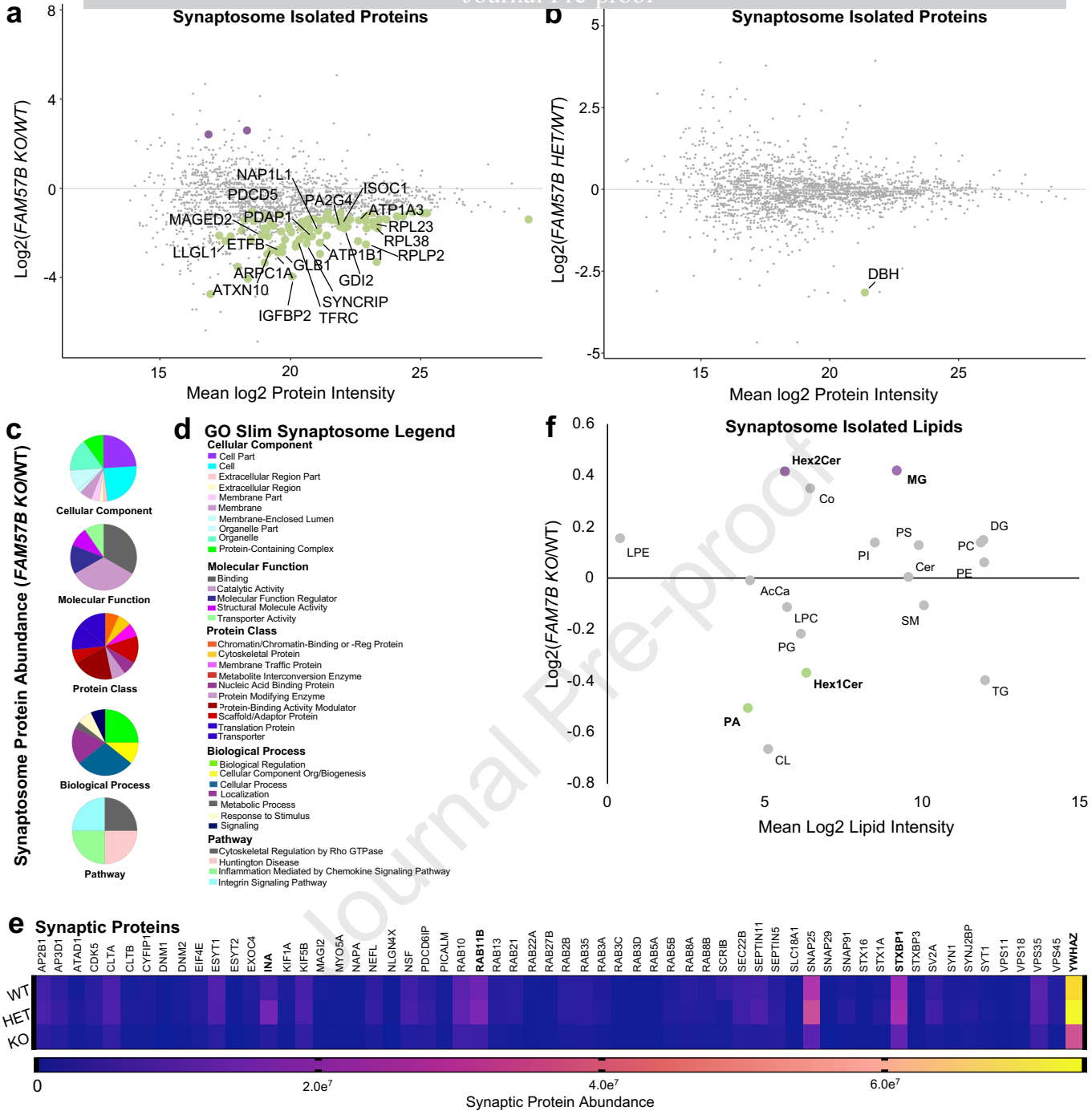

Figure 5. *FAM57B* knockout human neurons indicate altered synaptic composition.

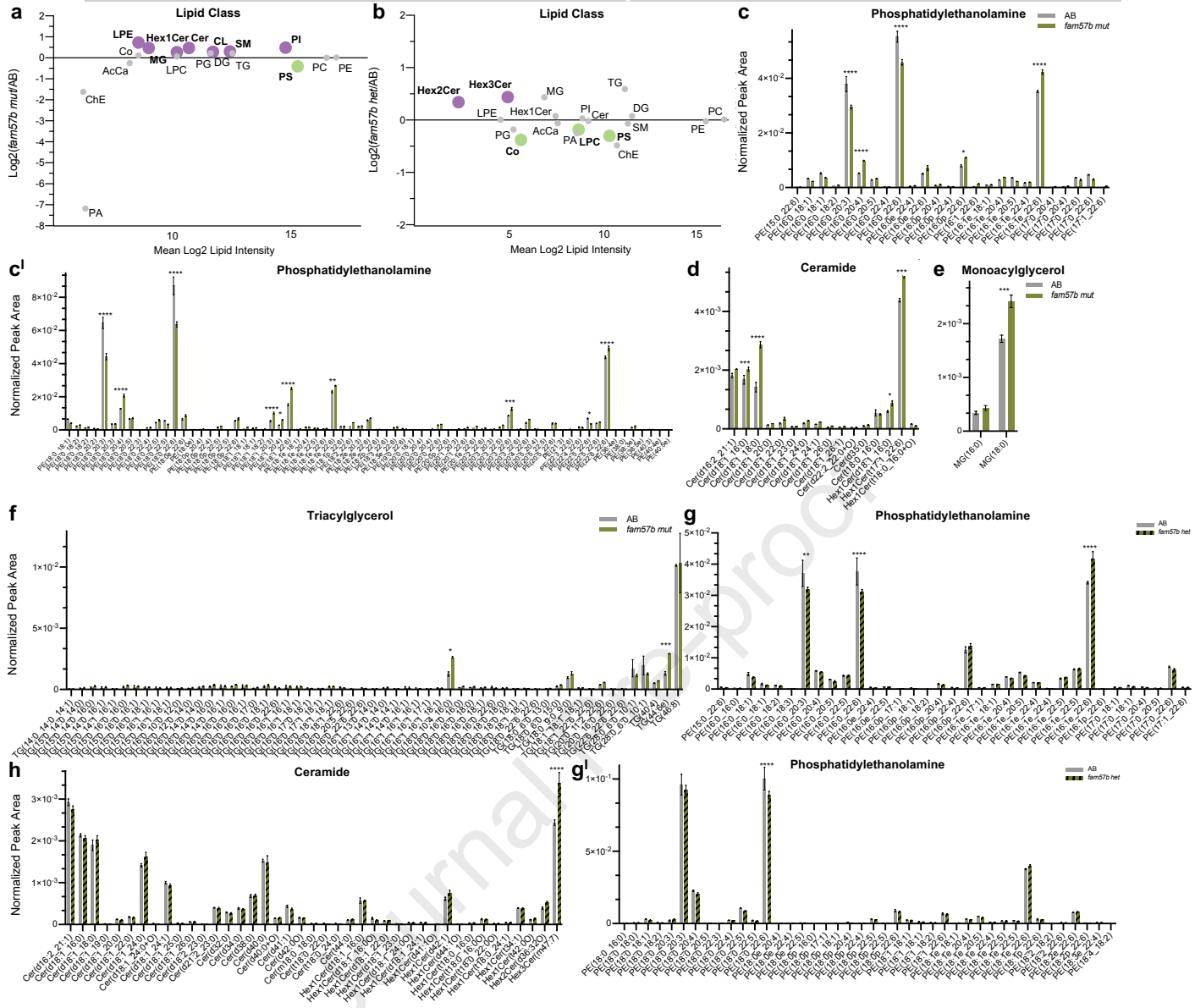

Figure 6. Significant lipid changes in ceramides and glycerols between AB and *fam57b mut* brain tissue.

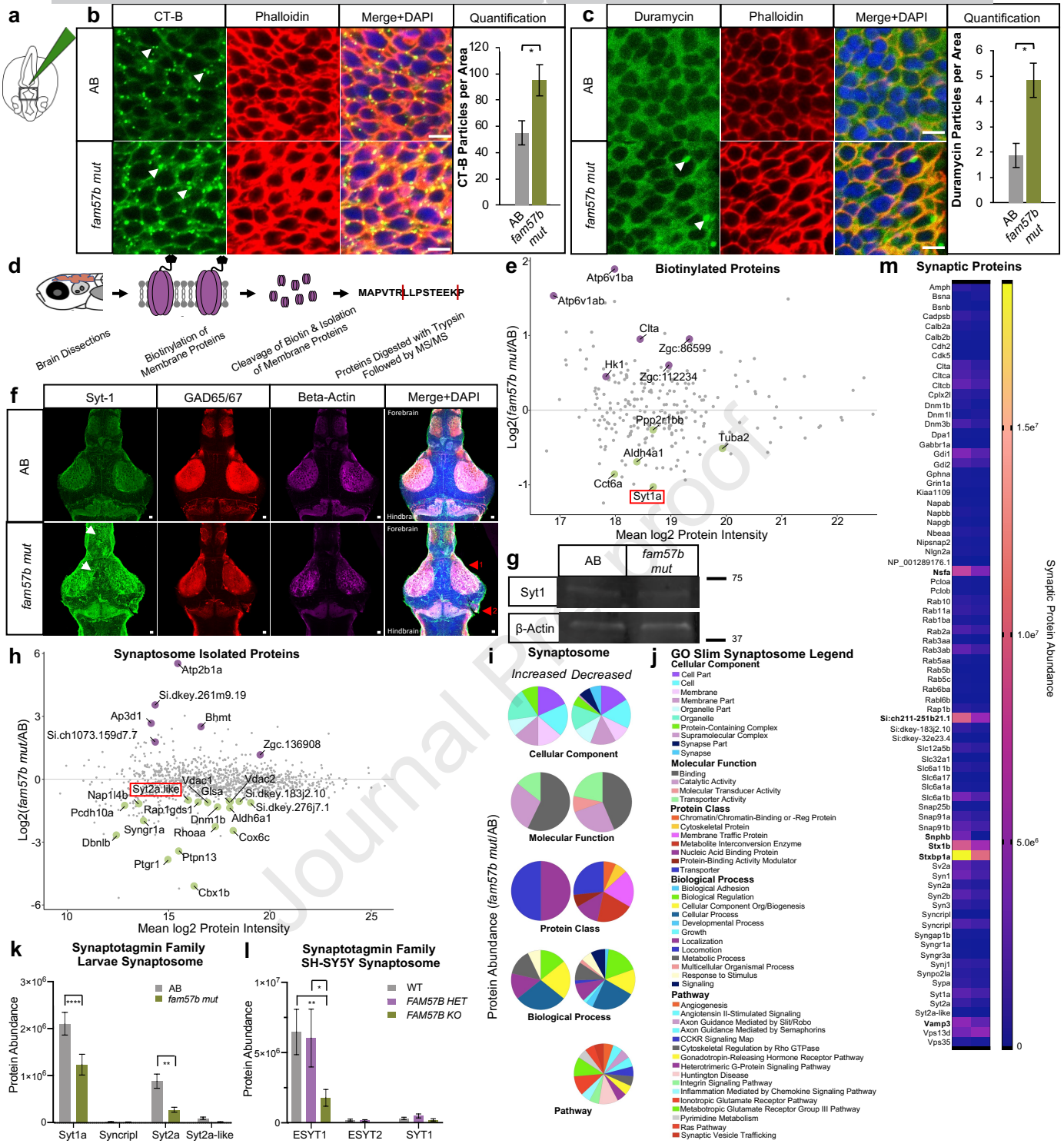

Figure 7. Loss of *fam57b* results in altered plasma membrane architecture early in development and decreased localization of Synaptotagmin family at the synapse later in development.

a

LFP and Burst Measurements	Burst Parameters 5 LFPs/100 ms			Decreased Burst Parameters 3 LFPs/200 ms		
	AB	*fam57b mut*	T-Test	AB	*fam57b mut*	T-Test
Sum of LFPs	1015	210		1015	210	
Ave Number of LFPs	7.463	3.088	*	7.463	3.088	*
Ave Mean LFP Rate (Hz)	0.012	0.005	*	0.012	0.005	*
Ave ILI Coefficient of Variation	1.244	1.021	**	1.244	1.021	**
Sum of Electrographic Bursts	29	0		82	3	
Ave Number of Electrographic Bursts	0.213	0		0.603	0.044	
Ave Electrographic Burst Duration	0.058	0		0.058	0.014	****
Ave Number of LFPs per Electrographic Burst	5.660	0		3.756	3	****
Ave Electrographic Burst Frequency (Hz)	0.006	0		0.005	0.002	**
Ave Electrographic Burst Percentage	2.442	0		9.414	1.548	**

b

Network Measurements	AB	*fam57b mut*	T-Test
Sum of Network Electrographic Bursts	127	26	
Ave Network Electrographic Bursts	6.684	1.857	*
Ave Network Electrographic Burst Frequency (Hz)	0.011	0.003	*
Ave Synchrony Index	0.440	0.318	

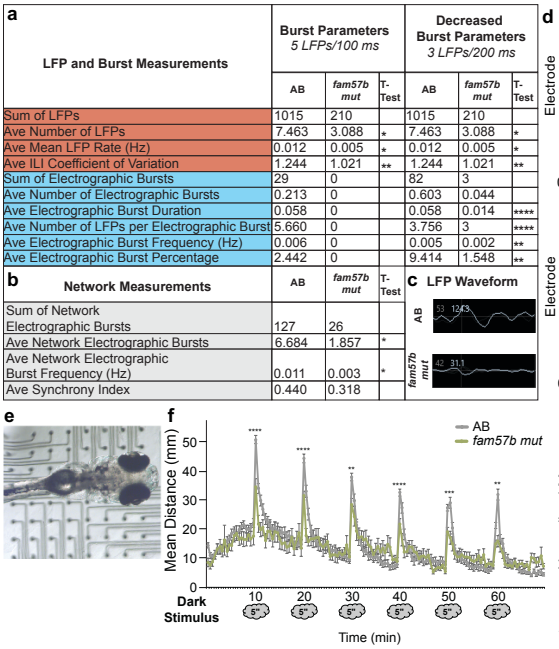

Figure 8. Decreased spontaneous brain activity and diminished behavioral response after stimuli presentation in *fam57b* mutants.

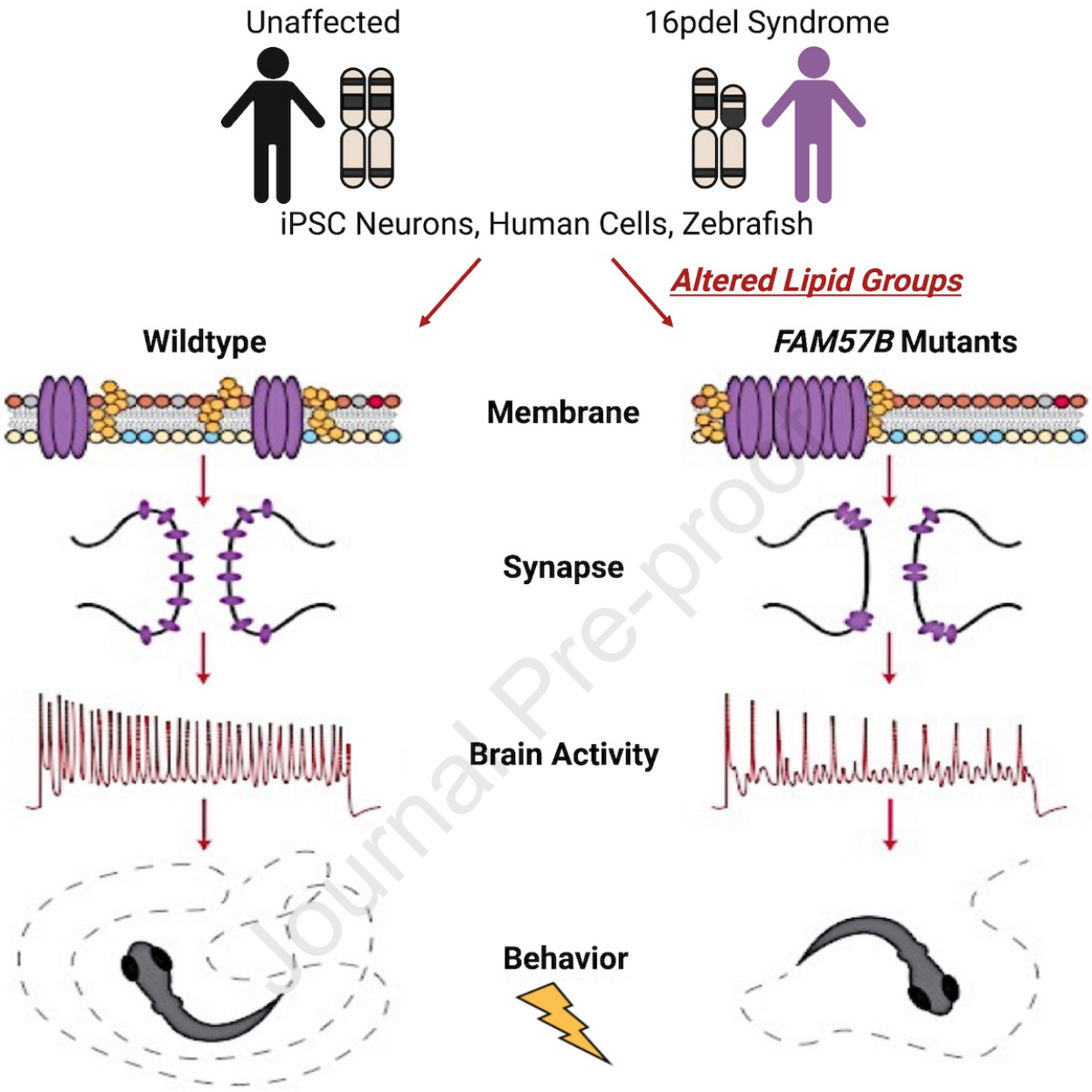

Highlights

- Augmented LFP activity and sex-specific differences in 16pdel neurons.
- 16pdel neuronal lipidome indicated altered ceramide related species.
- FAM57B is a ceramide synthase modulator essential for lipid regulation in the brain.
- FAM57B functions in synaptogenesis, synapse architecture and composition.